



# Characterizing Rocky and Gaseous Exoplanets with 2 m Class Space-based Coronagraphs

Tyler D. Robinson<sup>1,4,5</sup>, Karl R. Stapelfeldt<sup>2</sup>, and Mark S. Marley<sup>3</sup>

<sup>1</sup> Department of Astronomy and Astrophysics, University of California, Santa Cruz, CA 95064, USA; [tydrobin@ucsc.edu](mailto:tydrobin@ucsc.edu)

<sup>2</sup> Exoplanets and Stellar Astrophysics Laboratory, NASA Goddard Space Flight Center, Code 667, Greenbelt, MD 20771, USA

<sup>3</sup> NASA Ames Research Center, MS 245-3, Moffett Field, CA 94035, USA

Received 2015 July 1; accepted 2015 November 12; published 2016 January 18

## Abstract

Several concepts now exist for small, space-based missions to directly characterize exoplanets in reflected light. While studies have been performed that investigate the potential detection yields of such missions, little work has been done to understand how instrumental and astrophysical parameters will affect the ability of these missions to obtain spectra that are useful for characterizing their planetary targets. Here, we develop an instrument noise model suitable for studying the spectral characterization potential of a coronagraph-equipped, space-based telescope. We adopt a baseline set of telescope and instrument parameters appropriate for near-future planned missions like WFIRST-AFTA, including a 2 m diameter primary aperture, an operational wavelength range of 0.4–1.0  $\mu\text{m}$ , and an instrument spectral resolution of  $\lambda/\Delta\lambda = 70$ , and apply our baseline model to a variety of spectral models of different planet types, including Earth twins, Jupiter twins, and warm and cool Jupiters and Neptunes. With our exoplanet spectral models, we explore wavelength-dependent planet–star flux ratios for main-sequence stars of various effective temperatures and discuss how coronagraph inner and outer working angle constraints will influence the potential to study different types of planets. For planets most favorable to spectroscopic characterization—cool Jupiters and Neptunes as well as nearby super-Earths—we study the integration times required to achieve moderate signal-to-noise ratio spectra. We also explore the sensitivity of the integration times required to either detect the bottom or presence of key absorption bands (for methane, water vapor, and molecular oxygen) to coronagraph raw contrast performance, exozodiacal light levels, and the distance to the planetary system. Decreasing detector quantum efficiency at longer visible wavelengths makes the detection of water vapor in the atmospheres of Earth-like planets extremely challenging, and also hinders detections of the 0.89  $\mu\text{m}$  methane band. Additionally, most modeled observations have noise dominated by dark currents, indicating that improving CCD performance could substantially drive down requisite integration times. Finally, we briefly discuss the extension of our models to a more distant future Large UV-Optical-Infrared (LUVOIR) mission.

**Key words:** astrobiology – planets and satellites: atmospheres – planets and satellites: detection – planets and satellites: gaseous planets – planets and satellites: terrestrial planets – techniques: spectroscopic

**Online material:** color figures

## 1. Introduction

Exoplanet atmospheric characterization is a rapidly progressing field and will likely continue on this trajectory as the detection and study of nearby exoplanets was highlighted as one of three main science objectives in the 2010 National Research Council decadal survey of astronomy and astrophysics.<sup>6</sup> Following the first detection of an exoplanet atmosphere (Charbonneau et al. 2002), secondary eclipse and transit observations have been used to characterize the atmospheres of a number of hot Jupiters (Grillmair et al. 2008; Pont et al. 2008;

Swain et al. 2008, 2009; Madhusudhan & Seager 2009; Sing et al. 2009). More recently, observations have begun to probe new categories of planets, including mini-Neptune and super-Earth exoplanets (Bean et al. 2010; Stevenson et al. 2010; Ehrenreich et al. 2014; Fraine et al. 2014; Knutson et al. 2014a, 2014b; Kreidberg et al. 2014). Of course, and as with any young field, some findings remain controversial or have undergone substantial revision (Line et al. 2014; Diamond-Lowe et al. 2014; Hansen et al. 2014).

Anticipating future exoplanet direct detection missions, several studies have investigated the detection capabilities of coronagraph or starshade instruments. Agol (2007) presented analytic models of the detection efficiency of coronagraph searches and investigated dependencies on key parameters,

<sup>4</sup> Sagan Fellow.

<sup>5</sup> NASA Astrobiology Institute’s Virtual Planetary Laboratory.

<sup>6</sup> [www.nationalacademies.org/astro2010](http://www.nationalacademies.org/astro2010)

including survey duration, telescope diameter, and telescope inner working angle (IWA). Brown & Soummer (2010) discussed methods for optimizing survey “completeness” (Brown 2004, 2005), while other studies (Savransky et al. 2010; Turnbull et al. 2012) have emphasized techniques for evaluating the effectiveness of proposed missions. Mawet et al. (2014) studied the statistics of high-contrast imaging at small angles and found that the limited number of resolution elements near to the star (i.e., at  $\lesssim 2\lambda/D$ ) can lead to large errors in contrast estimations and false-alarm probabilities computed by less sophisticated methods. Stark et al. (2014) presented an improved technique for optimizing exoplanet detection completeness and explored the dependencies of exo-Earth yield on a number of astrophysical, mission, and instrument parameters. In a follow-up paper, Stark et al. (2015) used their completeness model to compute lower limits on the aperture size required to find and characterize a significant number of Earth twins. Very recently, Greco & Burrows (2015) studied the detection capabilities of a coronagraph-equipped WFIRST-AFTA mission<sup>7</sup> (Spergel et al. 2013).

Technologies and ideas for direct detection and characterization of exoplanets have long been discussed, and there exists a body of white papers and summary documents that outline strategies for direct characterization missions (Beichman et al. 1999; Des Marais et al. 2002; Lunine et al. 2008; Schneider et al. 2008; Cockell et al. 2009). Recently, following a growing interest in exoplanet direct detection,<sup>8,9</sup> NASA’s Exoplanet Exploration Program commissioned a number of “quick study” reports focused on exoplanet characterization at visible wavelengths. Marley et al. (2014) discussed how reflected light observations could be used to characterize existing radial velocity-detected exoplanets. Hu (2014) studied how direct imaging could constrain methane abundances and cloud properties using low-resolution spectra. Finally, Burrows (2014) explored the diversity of giant exoplanet spectra that may be accessible to a coronagraph-equipped WFIRST-AFTA mission.

Only a subset of the aforementioned quick studies considered the influence of noise on spectral observations, which, if included, is commonly applied by assuming a constant signal-to-noise ratio (S/N) across the entire modeled “observation.” While some studies have done extensive modeling of the influence of speckle noise (and techniques for minimizing such noise) on direct exoplanet observations (Marois et al. 2000; Sparks & Ford 2002), few published studies exist that comprehensively examine how spectral observations are influenced by stellar leakage, zodiacal light, exozodiacal light, and other noise sources. Maire et al. (2012)

investigated how noise would influence the characterization capabilities of the proposed Spectro-Polarimetric Imaging and Characterization of Exoplanetary Systems (SPICES) mission (Boccaletti et al. 2012). This work included noise due to speckles, exozodiacal light, zodiacal light, and readout, resulting in a handful of spectral simulations for planet–star systems for a specified distance and integration time. Recently, Leger et al. (2015) studied design missions for a 2 m class space-based coronagraph mission and a four-spacecraft formation flying interferometer mission, assuming noise from only stellar leakage and exozodiacal light, with a primary goal of determining how effective such missions would be in studying exo-Earths given new estimates of  $\eta_{\oplus}$ .

Here, we build on the limited previous studies of the influence of noise on the ability of space-based coronagraphs to characterize exoplanets. We begin by outlining a framework for modeling noise for such missions, including stellar leakage, exozodiacal light, zodiacal light, dark current, and read noise. We then investigate the capabilities of a 2 m class mission to observe and study a variety of Jupiter- and Neptune-sized worlds as well as terrestrial exoplanets. Using a characteristic set of mission parameters, we show how expected integration times will scale with wavelength and host star spectral type, and, for key spectral features, we show the sensitivity of these integration times to distance to the star–planet system, exozodiacal light levels, and coronagraph raw contrast performance. Finally, we discuss how our framework extends to the characterization of Earth twins with Large UV-Optical-InfraRed (LUVOIR) telescope missions.

## 2. Model Description

We consider a space-based telescope of diameter  $D$  designed to detect and characterize exoplanets in reflected light. The telescope is equipped with a coronagraph that achieves a raw contrast  $C$  (which can, in general, be wavelength-dependent) and has inner and outer working angles of  $\theta_{\text{IWA}}$  and  $\theta_{\text{OWA}}$ , respectively. The planetary light is distributed into a point-spread function (PSF), where an aperture of width (or diameter)  $X\lambda/D$  is used in the image plane to extract the planetary signal. However, a number of other sources will contribute to the detector counts within the defined aperture, including Solar System zodiacal light, exozodiacal light, leaked stellar light, dark current, and read noise.

The Appendix contains a presentation of our models of the planet count rate and count rates from key noise sources, which are similar to those of Brown (2005). For convenience, a synopsis of all of the model parameters, variables, and outputs are given in Table 1. Briefly, our planet count rate ( $c_p$ ), zodiacal light count rate ( $c_z$ ), exozodiacal light count rate ( $c_{ez}$ ), stellar leakage count rate ( $c_{lk}$ ), dark current count rate ( $c_D$ ), and read noise count rate ( $c_R$ ) are computed using Equations (13), (15), (17), (19), (20), and (29), respectively.

<sup>7</sup> [http://wfirst.gsfc.nasa.gov/science/std\\_public/WFIRST-AFTA\\_SDT\\_Report\\_150310\\_Final.pdf](http://wfirst.gsfc.nasa.gov/science/std_public/WFIRST-AFTA_SDT_Report_150310_Final.pdf)

<sup>8</sup> [http://exep.jpl.nasa.gov/stdt/Exo-C\\_Final\\_Report\\_for\\_Unlimited\\_Release\\_150323.pdf](http://exep.jpl.nasa.gov/stdt/Exo-C_Final_Report_for_Unlimited_Release_150323.pdf)

<sup>9</sup> [http://exep.jpl.nasa.gov/stdt/Exo-S\\_Starshade\\_Probe\\_Class\\_Final\\_Report\\_150312\\_URS250118.pdf](http://exep.jpl.nasa.gov/stdt/Exo-S_Starshade_Probe_Class_Final_Report_150312_URS250118.pdf)

**Table 1**  
Symbol Usage

Symbol	Description
$A$	wavelength-dependent planetary geometric albedo
$\alpha$	planet phase angle
$B_\lambda$	Planck function
$C$	coronagraph design contrast
$C_{\text{noise}}$	total number of noise counts on detector for a spectral element
$C_b$	total number of background counts on detector for a spectral element
$C_{\text{tot}}$	total number of counts on detector for a spectral element
$c_b$	total background count rate on detector for a spectral element
$c_{\text{tot}}$	total count rate on detector for a spectral element
$c_D$	dark current count rate on detector
$c_{\text{ez}}$	exozodiacal light count rate on detector
$c_p$	planetary count rate on detector
$c_R$	read noise count rate on detector
$c_{\text{lk}}$	leakage count rate on detector
$c_z$	zodiacal light count rate on detector
$c$	speed of light
$D$	telescope diameter
$D_{\text{e}^-}$	dark current
$d$	distance to observed star-planet system
$F_{p,\lambda}$	planetary specific flux
$F_{s,\lambda}$	stellar specific flux
$F_{\odot,\lambda}$	solar specific flux
$F_{\odot,V}$	V-band solar specific flux
$F_{s,V}$	V-band stellar specific flux
$F_{0,V}$	standard zero-magnitude V-band specific flux
$f_{\text{pa}}$	fraction of planetary light that falls within photometric aperture
$h$	Planck constant
$\lambda$	wavelength
$\Delta\lambda$	spectral element width
$M_{z,V}$	V-band zodiacal light surface brightness
$M_{\text{ez},V}$	V-band exozodiacal light surface brightness
$N_{\text{ez}}$	number of exozodis in exoplanetary disk
$N_{\text{read}}$	number of detector reads per observation
$N_{\text{pix},i/s}$	number of contributing pixels for imaging/spectroscopy
$\Delta N_{\text{hpix}}$	number of horizontal/spatial pixels for dispersed spectrum
$n_{\text{pix}}$	pixels per unit wavelength at detector for each lenslet spectrum
$\Omega$	photometry aperture size, expressed as $(X\lambda/D)^2$
$\Phi(\alpha)$	wavelength- and phase-dependent planetary phase function
$q$	detector quantum efficiency
$\mathcal{R}$	instrument spectral resolution
$R_p$	planetary radius
$R_s$	stellar radius
$R_{\text{e}^-}$	read noise counts per pixel
$r$	planet-star distance
$S/N$	signal-to-noise ratio
$\mathcal{T}$	telescope and instrument throughput
$\theta_{\text{IWA}}$	coronagraph inner working angle
$\theta_{\text{OWA}}$	coronagraph outer working angle
$\theta_{\text{pix}}$	detector pixel angular diameter
$\theta_{\text{lens}}$	lenslet angular diameter
$T_{\text{eff}}$	stellar effective temperature
$\Delta t_{\text{exp}}$	exposure time
$\Delta t_{\text{max}}$	detector maximum exposure time
$X$	width of photometric aperture, as multiple of $\lambda/D$

## 2.1. Baseline Parameters and Input Data

It is useful to define a baseline set of astrophysical, telescope, and instrument parameters, though later sections of this paper will explore sensitivity to key variables (e.g., distance, exozodiacal light levels, and coronagraph raw contrast). Baseline astrophysical parameters are given in Table 2, while telescope and instrument parameters are in Table 3.

Regarding astrophysical parameters, we adopt the standard, empirically derived solar spectrum of Wehrli (1985). As mentioned in Section A.2, we use a surface brightness of  $M_{z,V} = 23 \text{ mag arcsec}^{-2}$  for Solar System zodiacal light. For exozodiacal light, we assume one zodi (i.e.,  $N_{\text{ez}} = 1$ ) with a surface brightness of  $M_{\text{ez},V} = 22 \text{ mag arcsec}^{-2}$ , which is a factor of  $\sim 2$  larger than Solar System zodiacal surface brightness, as exozodiacal dust both above and below the midplane contribute (Stark et al. 2014).

For baseline telescope and instrument parameters, we consider a 2 m class telescope equipped with a coronagraph designed to achieve a raw contrast of  $C = 10^{-9}$  between  $\theta_{\text{IWA}} = 2\lambda/D$  and  $\theta_{\text{OWA}} = 10\lambda/D$ . The total system throughput is  $\mathcal{T} = 0.05$ , and we mimic the decreasing sensitivity of CCDs at red wavelengths by parameterizing the quantum efficiency according to

$$q = \begin{cases} 0.9, & \lambda \leq 0.7 \mu\text{m} \\ 0.9 \left( 1 - \frac{\lambda - 0.7}{0.3} \right), & 0.7 \mu\text{m} < \lambda \leq 1 \mu\text{m}. \end{cases} \quad (1)$$

We use a characteristic dark current of  $5 \times 10^{-4} \text{ s}^{-1}$  and read noise of 0.1. We assume a square aperture width of  $1.5\lambda/D$  (i.e.,  $X = 1.5$ ), which would be a sensible choice to help eliminate sensitivity to the sub-pixel (or sub-lenslet) location of the planet, whose PSF is sampled at  $0.5\lambda/D$ . Finally, we assume that the coronagraph is paired with a spectrometer that covers  $0.4\text{--}1.0 \mu\text{m}$  at  $\mathcal{R} = 70$ , which is sufficient to resolve many molecular absorption bands and features throughout the visible wavelength range (see Figure 1). Note that while a resolution of 70 is small enough to resolve the A-band of molecular oxygen, this may not be the ideal resolution for detecting this band (Brandt & Spiegel 2014). Overall, our assumed parameters are meant to be representative of either the previously mentioned WFIRST-AFTA mission or the Exo-C mission concept (see reports linked in the Introduction).

Our reflectivity data come from a number of different sources. For Earth twins we use the extensively validated Virtual Planetary Laboratory 3D spectral Earth model from Robinson et al. (2011), which realistically simulates wavelength- and phase-dependent spectra of the Pale Blue Dot (Robinson et al. 2010, 2014). In certain cases, we investigate super-Earths, which we take to have an Earth-like reflectivity and a radius of  $1.5 R_{\oplus}$ , and Venus twins, with a characteristic reflectivity from the validated models of Arney et al. (2014).

**Table 2**  
Baseline Astrophysical Parameter Values

Parameter	Description	Adopted Value
$\alpha$	planet phase angle	$90^\circ$
$F_{0, V}$	standard zero-magnitude V-band specific flux	$3.63 \times 10^{-8} \text{ W m}^{-2} \mu\text{m}^{-1}$
$M_{z, V}$	V-band zodiacal light surface brightness	$23 \text{ mag arcsec}^{-2}$
$M_{ez, V}$	V-band exozodiacal light surface brightness	$22 \text{ mag arcsec}^{-2}$
$N_{ez}$	number of exozodis in exoplanetary disk	1

**Table 3**  
Baseline Telescope and Instrument Parameter Values

Parameter	Description	Adopted Value
$C$	coronagraph design contrast	$10^{-9}$
$D_e^-$	dark current	$5 \times 10^{-4} \text{ s}^{-1}$
$D$	telescope diameter	2 m
$f_{pa}$	fraction of planetary light that falls within photometric aperture	0.87
$\Delta N_{\text{hpix}}$	number of horizontal/spatial pixels for dispersed spectrum	3
$q$	detector quantum efficiency	Equation (1)
$\mathcal{R}$	instrument spectral resolution	70
$R_e^-$	read noise counts per pixel	0.1
$\mathcal{T}$	telescope and instrument throughput	0.05
$\theta_{\text{IWA}} (\lambda/D)$	coronagraph inner working angle	2
$\theta_{\text{OWA}} (\lambda/D)$	coronagraph outer working angle	10
$\Delta t_{\text{max}}$	detector maximum exposure time	1 hr
$X$	width of photometric aperture, as multiple of $\lambda/D$	1.5

For Jupiter and Neptune twins, we use the observed geometric albedos from Karkoschka (1998) and a Lambertian phase function given by

$$\Phi_L(\alpha) = \frac{\sin \alpha + (\pi - \alpha) \cos \alpha}{\pi}, \quad (2)$$

although realistic planetary phase functions are not perfectly Lambertian (e.g., Cahoy et al. 2010, their Figure 15). Recall that the phase function captures phase-dependent brightness changes as the planet moves through its orbit and that the brightness increase from quadrature to full phase is a factor of  $\sim 3$ . Finally, we also consider “warm” and “cool” Jupiters and Neptunes, using the wavelength- and phase-dependent models of Cahoy et al. (2010) for both a 0.8 and 2 AU (from a Sun-like star) Jupiter and Neptune (at  $3\times$  and  $30\times$  heavy element enhancement, respectively). All planets are taken to be at a characteristic phase angle of  $\alpha = \pi/2 = 90^\circ$  (i.e., quadrature).

## 2.2. Noise

The total number of counts,  $C_{\text{tot}}$ , is computed from the total count rate using

$$\begin{aligned} C_{\text{tot}} &= (c_p + c_z + c_{ez} + c_{\text{lk}} + c_D + c_R) \Delta t_{\text{exp}} \\ &= (c_p + c_b) \Delta t_{\text{exp}}, \end{aligned} \quad (3)$$

where  $\Delta t_{\text{exp}}$  is the exposure time, and we have defined the total background count rate,  $c_b = c_z + c_{ez} + c_{\text{lk}} + c_D + c_R$ . The total number of background counts would be  $C_b = c_b \Delta t_{\text{exp}}$ . Following Brown (2005), the noise counts are taken as

$$C_{\text{noise}} = \sqrt{C_p + 2C_b}, \quad (4)$$

which assumes a background subtraction (e.g., via a spacecraft roll maneuver) is performed to detect the planet (implying that the single-exposure photon counting noise limit is not achieved), and  $C_p$  is the total planet counts. With the S/N given by

$$S/N = \frac{C_p}{C_{\text{noise}}}, \quad (5)$$

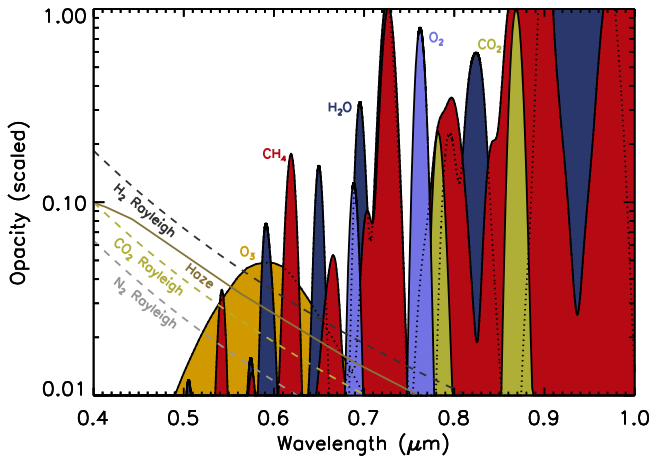


**Figure 1.** Scaled opacities for different species and aerosols between 0.4 and  $1.0 \mu\text{m}$  at  $\mathcal{R} = 70$ , demonstrating the numerous bands and features present across the visible wavelength range. Scalings for gaseous absorption are constant with wavelength for each species and arbitrary; these were chosen to highlight relevant bands. The haze opacity is for extinction by a Titan tholin-like haze, and the Rayleigh scattering opacities are scaled to that of  $\text{CO}_2$  at  $0.4 \mu\text{m}$  (and divided by 10).

(A color version of this figure is available in the online journal.)



we can compute the exposure time needed to achieve a given S/N by

$$\Delta t_{\text{exp}} = \frac{c_p + 2c_b}{c_p^2} S/N^2. \quad (6)$$

Note that the exposure time required to achieve a given S/N is distinct from the S/N required to detect a certain molecule (e.g., Brandt & Spiegel 2014) or to distinguish between models with different heavy element enhancements (Maire et al. 2012). The former (given by Equation (6)), when applied at the bottom of several molecular features (as is done in later sections), is representative of the requisite exposure time for determining molecular abundances and cloud properties for exoplanet atmosphere (Marley et al. 2014). Such determinations require comparisons to cloudy atmospheric models, both at continuum wavelengths and across/in molecular bands, thereby simultaneously retrieving cloud and atmospheric parameters (including the abundances of key species).

We also explore the integration time required to simply detect a molecular feature by the deviation it causes from a flat continuum, which is sufficient for stating whether or not a certain species is present in an atmosphere. Following Misra et al. (2014), we write the band S/N by defining the signal as the count difference between the spectral model and a model without absorption, determined by fitting the continuum on both sides of the absorption band. The noise counts are summed over the band. Thus, if  $c_{\text{cont}}$  is the continuum count rate, then the band S/N is given by

$$S/N_{\text{band}} = \frac{\sum_j c_{\text{cont},j} - c_{p,j}}{\sqrt{\sum_j c_{p,j} + 2c_{b,j}}} \Delta t_{\text{exp}}^{1/2}, \quad (7)$$

where the sum is over all spectral elements (denoted by subscript “ $j$ ”) within the molecular band. Band detection times, in general, will be long for shallow and narrow features, whereas the previously discussed exposure times to reach a given S/N at the bottom of a band is shortest for shallow features. These two times will be roughly equal for a feature that is one resolution element in width and that is moderately deep.

### 3. Results

The following subsections explore the detectability of, and integration time required to detect, key spectral features for various categories of planets. We define a planet “type” as having a fixed radius, reflectivity [ $A\Phi(\alpha)$ ], and incident flux from its host star. The latter requirement is sometimes referred to as the “flux (or insolation) equivalent distance.” Note that we focus on the visible wavelength range (0.4–1.0  $\mu\text{m}$ ), as exoplanet characterization in reflected light at near-infrared wavelengths is especially difficult for small telescopes due to IWA constraints.

To get a sense for the scales involved, we note that an Earth twin around a Sun-like star, using  $A = 0.2$ ,  $\Phi(\pi/2) \sim 1/\pi$ ,  $R_p = R_\oplus$ , and  $r = 1 \text{ AU}$ , would have the canonical planet–star flux ratio (from Equation (11)) of  $10^{-10}$ . Then, assuming our baseline parameters, and using  $\lambda = 0.55 \mu\text{m}$  with a 8 nm wide bandpass, Equation (13) gives  $c_p \sim 5 \times 10^{-4} \text{ s}^{-1}$  (or about  $2 \text{ hr}^{-1}$ ) for an Earth twin at 5 pc. By comparison, the leakage count rate is  $20 \text{ hr}^{-1}$  for  $C = 10^{-9}$ , while the zodiacal and exozodiacal light count rates are 2 and  $4 \text{ hr}^{-1}$ , respectively. With a dark count rate of about  $240 \text{ hr}^{-1}$  and a read noise count rate of  $10 \text{ hr}^{-1}$ , the exposure time needed to reach  $S/N = 5$  is roughly  $5 \times 10^3 \text{ hr}$ —an unfeasibly long integration time, but which could be reduced by decreasing spectral resolution. For a Jupiter twin at 5 pc, with a geometric albedo of 0.5, the planet–star flux ratio increases to  $\sim 10^{-9}$ , and the planet count rate increases to  $20 \text{ hr}^{-1}$  (although this twin, at 5.2 AU from its Sun-like host, would be outside  $\theta_{\text{OWA}} = 10\lambda/D$  at quadrature) while the exozodiacal light count rate decreases to  $0.2 \text{ hr}^{-1}$ . Here, then, the time needed to reach  $S/N = 5$  is only 30 hr.

As demonstrated by these count rate example calculations, the dominant term in the noise counts (Equation (4))—for a wide range of planet types, distances, stellar effective temperatures, and wavelengths—is dark current. This term is strongly influenced by two parameters: the dark current rate ( $D_e$ ) and the width of our assumed photometric aperture (controlled by  $X$ ). The latter term determines the area used to extract the planetary signal, which leads to a  $X^2$  dependence in the dark noise count rate. For our assumed baseline set of parameters and a characteristic distance of 10 pc, all of the planet types investigated in Section 3.2 and later have dark current as the dominant noise source, leading the exposure times required to achieve a given S/N to scale with the planet count rate as (roughly)  $c_D/c_p^2$ . Note that this scaling leads to a strong dependence on planetary properties, implying that, for example, observing planets closer to full phase would drive down integration times by as much as an order of magnitude from the estimates provided below (which are given at quadrature phase). Also, the overall importance of dark current in our results below is influenced by our baseline throughput assumption (selected to be consistent with, e.g., WFIRST-AFTA)—improved telescope and instrument throughputs will drive up the planetary signal, while also increasing the relative weights of noise due to stellar leakage and zodiacal and exozodiacal light.

#### 3.1. Planet–Star Flux Ratios

Insight into the complexities associated with directly observing cool exoplanets comes from investigating planet–star flux ratios for our different types of worlds. The first panel of Figure 2 shows the planet–star flux ratio as color contours for a Jupiter-sized world with  $A\Phi(\alpha) = 0.5/\pi$  (independent of wavelength) and with a Jupiter-like top-of-atmosphere flux

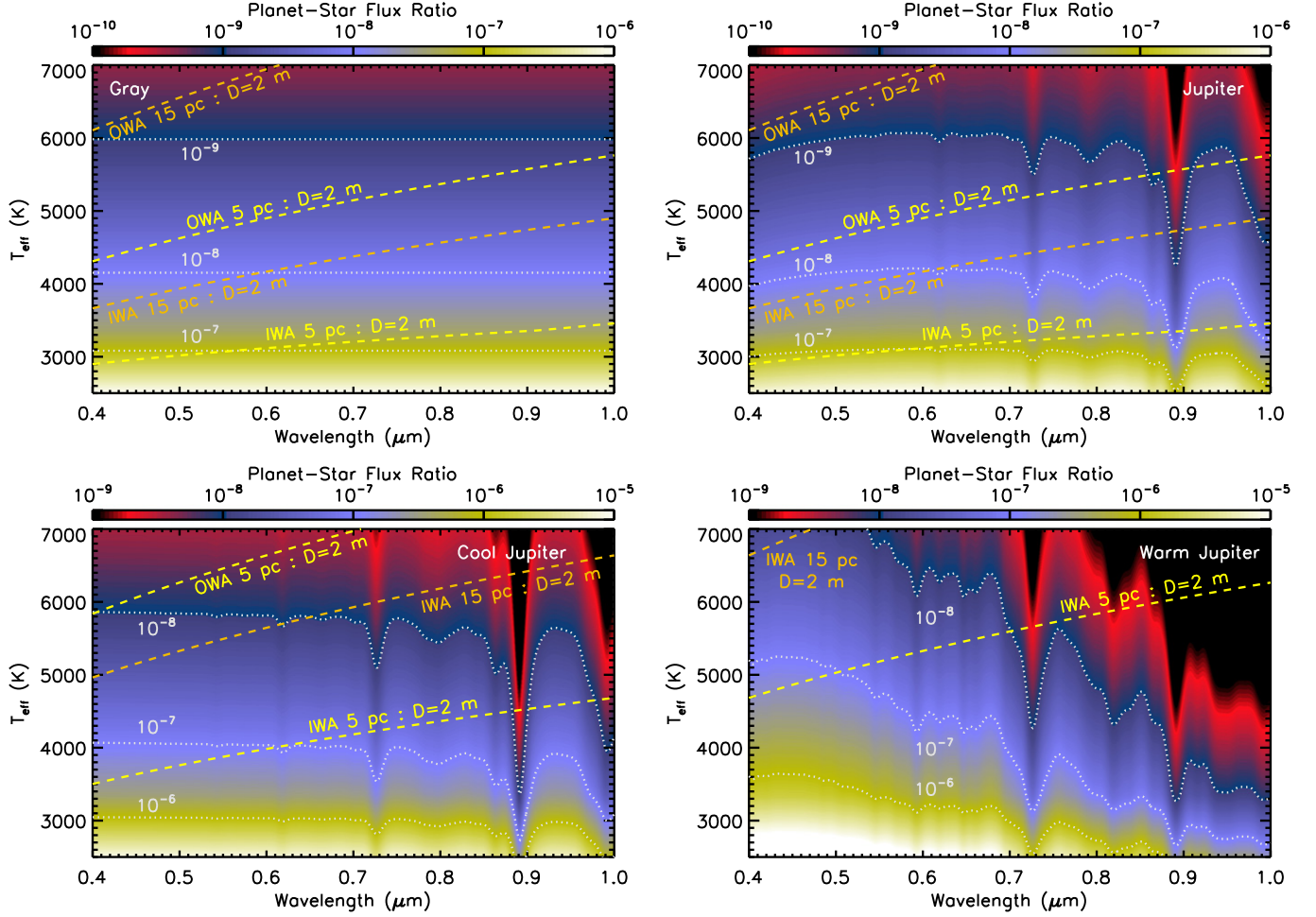


**Figure 2.** Planet–star flux ratio color contours for a variety of Jupiter-sized worlds at fixed flux equivalent distances around main-sequence stars of different effective temperatures. Planet types are: (a) a gray planet with  $A\Phi(\alpha) = 0.5/\pi$  and  $F_{\text{TOA}} = 50.5 \text{ W m}^{-2}$  (top left), (b) a Jupiter twin with  $F_{\text{TOA}} = 50.5 \text{ W m}^{-2}$  and reflectivity from Karkoschka (1998; top right), (c) a cool Jupiter with  $F_{\text{TOA}} = 342 \text{ W m}^{-2}$  and reflectivity from Cahoy et al. (2010; bottom left), and (d) a warm Jupiter with  $F_{\text{TOA}} = 2140 \text{ W m}^{-2}$  and reflectivity from Cahoy et al. (2010; bottom right). Inner and outer working angle constraints (at quadrature; dashed), at  $2\lambda/D$  and  $10\lambda/D$ , are shown for a 2 m class telescope and assuming the planet–star systems are at 5 pc (yellow) and 15 pc (orange).

(A color version of this figure is available in the online journal.)

(fixed at  $F_{\text{TOA}} = 50.5 \text{ W m}^{-2}$ ), as a function of main-sequence host star effective temperature. As we have assumed a gray reflectivity, the planet–star flux ratio only depends on  $T_{\text{eff}}$  (assuming a simple relationship between this and  $R_s$  on the main sequence), with

$$\frac{F_p}{F_s} = \frac{A\Phi(\alpha)F_{\text{TOA}}}{\sigma T_{\text{eff}}^4} \left( \frac{R_p}{R_s} \right)^2, \quad (8)$$

where the dependence on planetary orbital distance is functionally removed. Here, since the planet flux is fixed by  $A\Phi(\alpha)$  and  $F_{\text{TOA}}$  (regardless of stellar effective temperature), the planet–star flux ratio increases for cooler stars as these stars are intrinsically fainter.

The planet–star flux ratio contours for the gray case in Figure 2 tell an incomplete story, however. First, while the results indicate that detecting a Jupiter-sized planet around cool stars (with  $T_{\text{eff}} < 4000 \text{ K}$ ) would be straightforward with a coronagraph capable of achieving a raw contrast of only  $10^{-8}$ , it is important to remember that the probability that such cool stars host a gas giant is small (of the order a few percent; Johnson et al. 2010; Montet et al. 2014). Additionally, the coronagraph inner and outer working angles will constrain the range of planet–star apparent separations (which are related to orbital separations) accessible to the telescope when observing a system at a given distance. These constraints are shown as dashed lines for distances of 5 and 15 pc in Figure 2. For fixed  $F_{\text{TOA}}$  and a system distance of 5 pc, the OWA would not allow

observations of the gray Jupiter world at quadrature over the entire wavelength range for host stars with effective temperatures above 5800 K. When placed at 15 pc, the IWA can prevent observations at the longest wavelengths for stars with an effective temperature below 4900 K.

The remaining panels in Figure 2 show non-gray cases, where realistic reflectivities are used. Like the gray case, the Jupiter twins have  $F_{\text{TOA}} = 50.5 \text{ W m}^{-2}$ , while the cool and warm Jupiters have  $F_{\text{TOA}} = 342 \text{ W m}^{-2}$  and  $F_{\text{TOA}} = 2140 \text{ W m}^{-2}$ , respectively. With the planet–star flux ratio now a function of wavelength, these plots allow us to easily determine roughly what raw contrast must be achieved to detect different types of Jupiters at continuum wavelengths and within absorption features. The Jupiter twins and the cool Jupiters are relatively reflective and have several methane bands covering a range of feature depths. Note that the Jupiter twins have low planet–star contrast ratios due to their small  $F_{\text{TOA}}$ . Additionally, despite their large  $F_{\text{TOA}}$ , the warm Jupiters have low planet–star contrast ratios at longer wavelengths due to strong methane and water vapor bands as well as a lack of water clouds.

Figure 3 is similar to Figure 2 but for Neptune twins, cool Neptunes, and warm Neptunes. Neptune twins have very low planet–star flux ratios due to a very small  $F_{\text{TOA}}$  ( $1.5 \text{ W m}^{-2}$ ) and would also be difficult to detect for a wide range of stellar effective temperatures due to the telescope OWA restrictions. The flux ratios improve for the cool and warm cases, but are lower than the equivalent Jupiter-sized cases as Neptune is 2.9 times smaller than Jupiter. Also, the methane and water bands for these cases are deeper than those for the Jupiters, yielding flux ratios near  $10^{-10}$ – $10^{-11}$  over much of parameter space.

Continuing downward in the size/mass regime, Figure 4 shows planet–star contrast ratios for Venus twins ( $F_{\text{TOA}} = 2610 \text{ W m}^{-2}$ ), as well as for Earth twins and super-Earths (both with  $F_{\text{TOA}} = 1370 \text{ W m}^{-2}$ ). The Venus twins have comparatively high planet–star flux ratios, both due to their high reflectivity and large  $F_{\text{TOA}}$ , and have nearly featureless spectra over the highlighted wavelength range. Inner working angle constraints make Venus twins very difficult to detect for our chosen architecture, especially at longer wavelengths. For Earths and super-Earths, the visible wavelength range contains key spectral features—the  $0.76 \mu\text{m}$   $\text{O}_2$  A-band and the  $0.94 \mu\text{m}$  water band—but IWA constraints largely limit our ability to characterize such planets around cool stars.

The relationships between wavelength-dependent reflectivity, host star effective temperature, and planet–star flux ratio discussed above can be straightforwardly manipulated to show contours of stellar effective temperature where planet types achieve a given flux ratio. Four such plots are shown in Figure 5, which illustrate the range of different stellar spectral types that can be investigated for a specified planet type and contrast performance. These diagrams demonstrate how, for a

fixed planet–star flux ratio, the depths of absorption bands can best be probed for cooler stars, where the low intrinsic stellar brightness compensates for the low planetary reflectivity. As before, inner and outer working angle limitations are shown for planet–star systems at 5 and 15 pc.

### 3.2. Integration Times: Full Spectral Range

We now shift our attention to the integration times required to achieve a specified S/N for different planet types. These exposure times determine whether or not it is realistically feasible to acquire the types of observations needed to characterize planets at a wide range of wavelengths, especially given constraints on mission duration and overall mission time allotted for exoplanet studies. While we highlight S/N = 5 as a minimum value needed for characterization—Marley et al. (2014) were able to draw scientifically valuable conclusions from their simulated data at this S/N—the exposure times discussed here can be easily scaled to other S/Ns since  $\Delta t_{\text{exp}} \propto \text{S/N}^2$ .

Wavelength-dependent integration times required to achieve S/N = 5 for fixed  $F_{\text{TOA}}$  cases are shown for Jupiter twins and cool Jupiters at a characteristic distance of 10 pc in Figure 6. Requisite integration times for the cool Jupiters are promising, reaching S/N = 5 in 10–100 hr, even in the depths of some methane absorption bands. For the Jupiter twins, detecting the bottom of these bands requires more than  $10^3$  hr of observation, owing to these planets’ larger orbital distances, although binning data to lower spectral resolution ( $\mathcal{R} = 20$ –30) would drive down the requisite exposure times (by a factor of a few).

Figure 7 shows integration times required to achieve S/N = 5 for cool Neptunes at a distance of 10 pc. Note that these integration times show a much larger dynamic range than the cool Jupiter cases owing to the generally deeper methane bands in the geometric albedo spectrum of the Neptunes. Overall, integration times shorter than  $10^3$  hr are only achieved below  $0.7 \mu\text{m}$ , owing to both strong absorption features and falling stellar spectra at longer wavelengths.

Finally, Figure 8 shows integration times to S/N = 5 for Earth twins and super-Earths, both taken to be at a 5 pc distance. To maintain integration times shorter than about  $10^3$  hr, the Earth and super-Earth observations have been degraded to spectral resolutions of 10 and 20, respectively (which would not allow detection of the  $0.76 \mu\text{m}$  A-band of molecular oxygen). Outside of the  $0.94 \mu\text{m}$  water band, the Earth twins have integration times of the order  $10^3$  hr, although achieving such observations for Sun-like stars and hotter would require a contrast noise floor better than  $10^{-10}$ . By comparison, super-Earths avoid the contrast limitation over most of parameter space and require integration times less than 500 hr for most wavelengths (at  $\mathcal{R} = 20$ ).



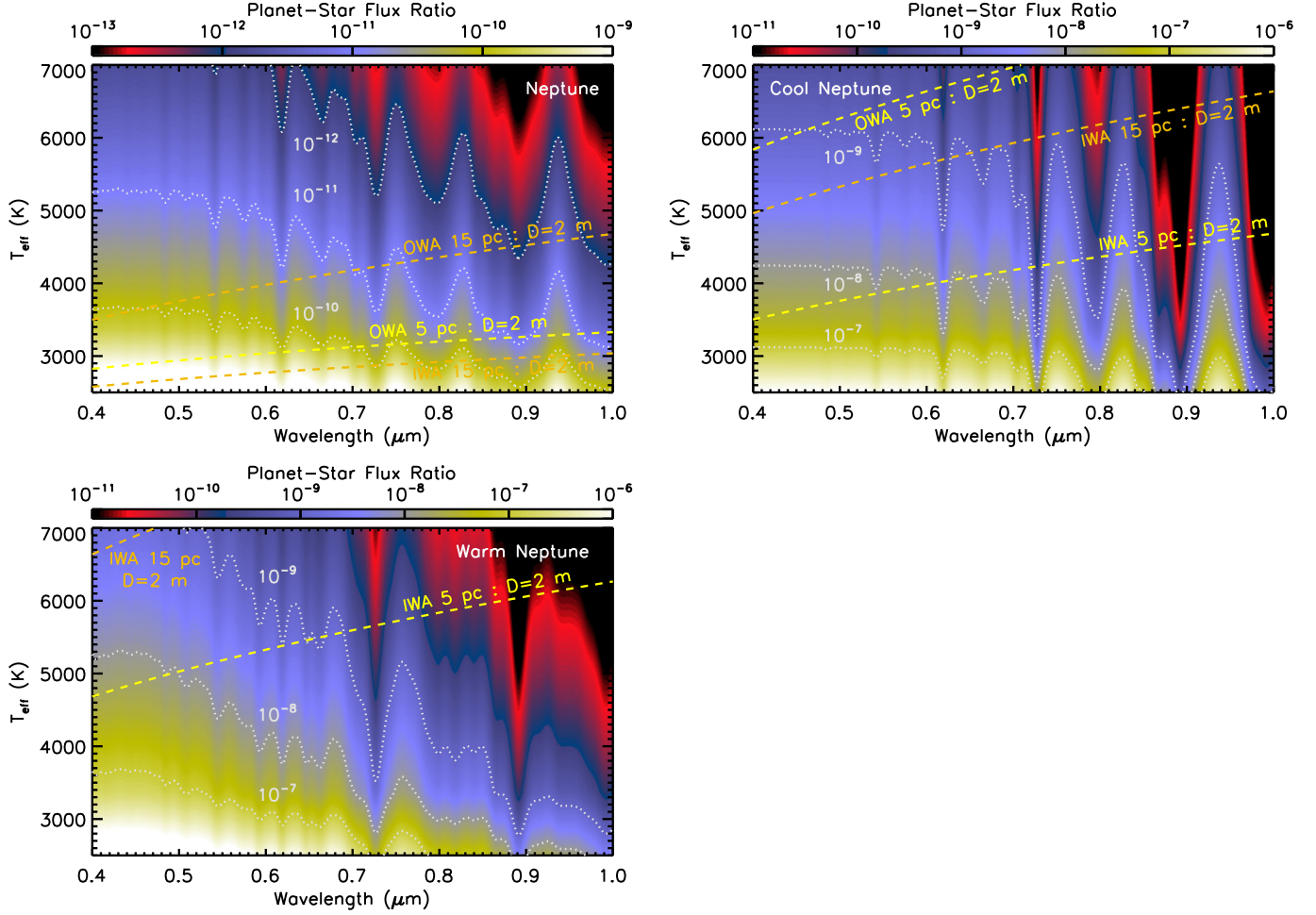


**Figure 3.** Same as Figure 2, but for Neptune-sized worlds. Planet types are: (a) a Neptune twin with  $F_{\text{TOA}} = 1.5 \text{ W m}^{-2}$  and reflectivity from Karkoschka (1998; top left), (b) a cool Neptune with  $F_{\text{TOA}} = 342 \text{ W m}^{-2}$  and reflectivity from Cahoy et al. (2010; top right), and (c) a warm Neptune with  $F_{\text{TOA}} = 2140 \text{ W m}^{-2}$  and reflectivity from Cahoy et al. (2010; bottom left). Inner and outer working angle constraints are also as in Figure 2. (A color version of this figure is available in the online journal.)

### 3.3. Integration Times: Molecular Features

By highlighting key molecular bands in certain planet-type spectra, we can investigate the integration times required to detect these features. We explore both the integration time required to achieve a given S/N at the bottom of a molecular band (Equation (6)), and the integration time required to detect a band (or bands) of certain species (Equation (7)). Recall that the former is indicative of the integration time required to achieve observations suitable for abundance determinations (where detections of the bottoms of multiple bands are required), while the latter indicates the time required to determine whether or not a species is present. As before, we set the detection S/N to be 5, which can easily be scaled to other S/N values. Also, for all the bands discussed below, our baseline spectral resolution ( $\mathcal{R} = 70$ ) is sufficient to resolve these bands (Des Marais et al. 2002).

Figure 9 shows integration times for detection of species and bottoms of bands for cool Jupiters as a function of distance to the planetary system. We focus on methane, which is the dominant absorber for the cool Jupiters (and Neptunes) at visible wavelengths. For detecting the bottoms of bands, we highlight the  $0.73 \text{ } \mu\text{m}$  and  $0.89 \text{ } \mu\text{m}$  methane bands, which are, respectively, moderate and strong bands. For detecting methane, we use the  $0.73 \text{ } \mu\text{m}$  band, although required integration times for detecting the  $0.89 \text{ } \mu\text{m}$  band are similar, owing to a tradeoff between detector quantum efficiency (lower at these wavelengths) and band strength (higher). We also show that the integration time required to detect methane is decreased by about 50% if both bands are used. Including the  $0.62 \text{ } \mu\text{m}$  methane band does not further decrease integration times, as the shallowness of this band leads to long required integration times for detection.

Figure 10 is similar to Figure 9, except for cool Neptunes. For detecting band bottoms, we use the  $0.54 \text{ } \mu\text{m}$  and



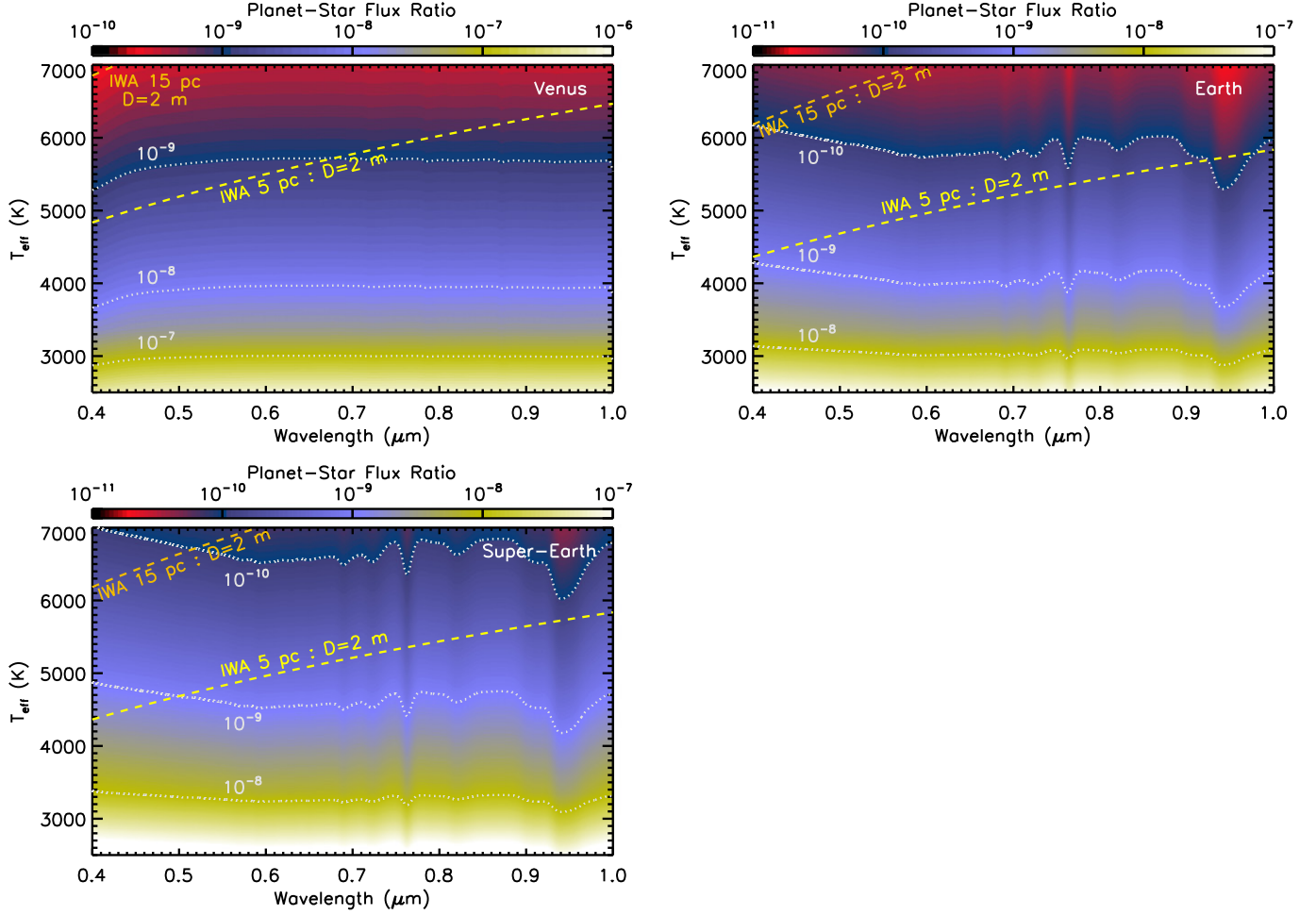


**Figure 4.** Same as Figure 2, but for terrestrial worlds. Planet types are: (a) a Venus twin with  $F_{\text{TOA}} = 2610 \text{ W m}^{-2}$  and reflectivity from an application of a line-by-line radiative transfer model (Meadows & Crisp 1996) to Venus (Arney et al. 2014; top left) (b) an Earth twin with  $F_{\text{TOA}} = 1370 \text{ W m}^{-2}$  and reflectivity from Robinson et al. (2010; top right), and (c) a super-Earth with  $1.5 R_{\oplus}$ ,  $F_{\text{TOA}} = 1370 \text{ W m}^{-2}$  and Earth-like reflectivity from Robinson et al. (2010; bottom left). Inner and outer working angle constraints are also as in Figure 2.

(A color version of this figure is available in the online journal.)

$0.62 \mu\text{m}$  methane bands, as detecting the bottom of longer wavelength bands would require a contrast noise floor smaller than  $10^{-10}$ . We show integration times for methane detection using the  $0.62 \mu\text{m}$  band and including both this band and the  $0.73 \mu\text{m}$  decreases requisite times by about 50%.

Finally, Figures 11 and 12 show integration times for band bottom and species detections for Earth twins and super-Earths, respectively. Here, we emphasize the  $0.76 \mu\text{m}$  A-band of molecular oxygen and the  $0.94 \mu\text{m}$  water vapor band. The A-band is a key potential biosignature, while the water vapor band is essential for discerning planetary habitability. Note that the time required to detect the bottom of the A-band is much shorter than the time to detect the presence of the band. This is due to the convolution of the high-resolution Earth reflectance spectrum with the spectrometer line-shape function, which serves to decrease the depth of this band at  $\mathcal{R} = 70$  and, thus,

makes detection of the band difficult. Thus, the integration time required to reach the bottom of the A-band at an S/N of 5 is not much different from the time to reach the same S/N in the surrounding continuum. We note that requisite integration times for Earths or super-Earths placed at the outer edge of the habitable zone are typically 5–10 times longer due to the lower stellar flux incident on these planets.

### 3.4. Sensitivity to Key Parameters

Our baseline parameter set assumed that every planet-star system has one exozodi and that the coronagraph could deliver a raw contrast of  $10^{-9}$ . However, exozodi levels can vary by orders of magnitude, as can the designed raw contrast (depending on which mission architecture is adopted). Thus, we explore sensitivity to these two parameters by examining

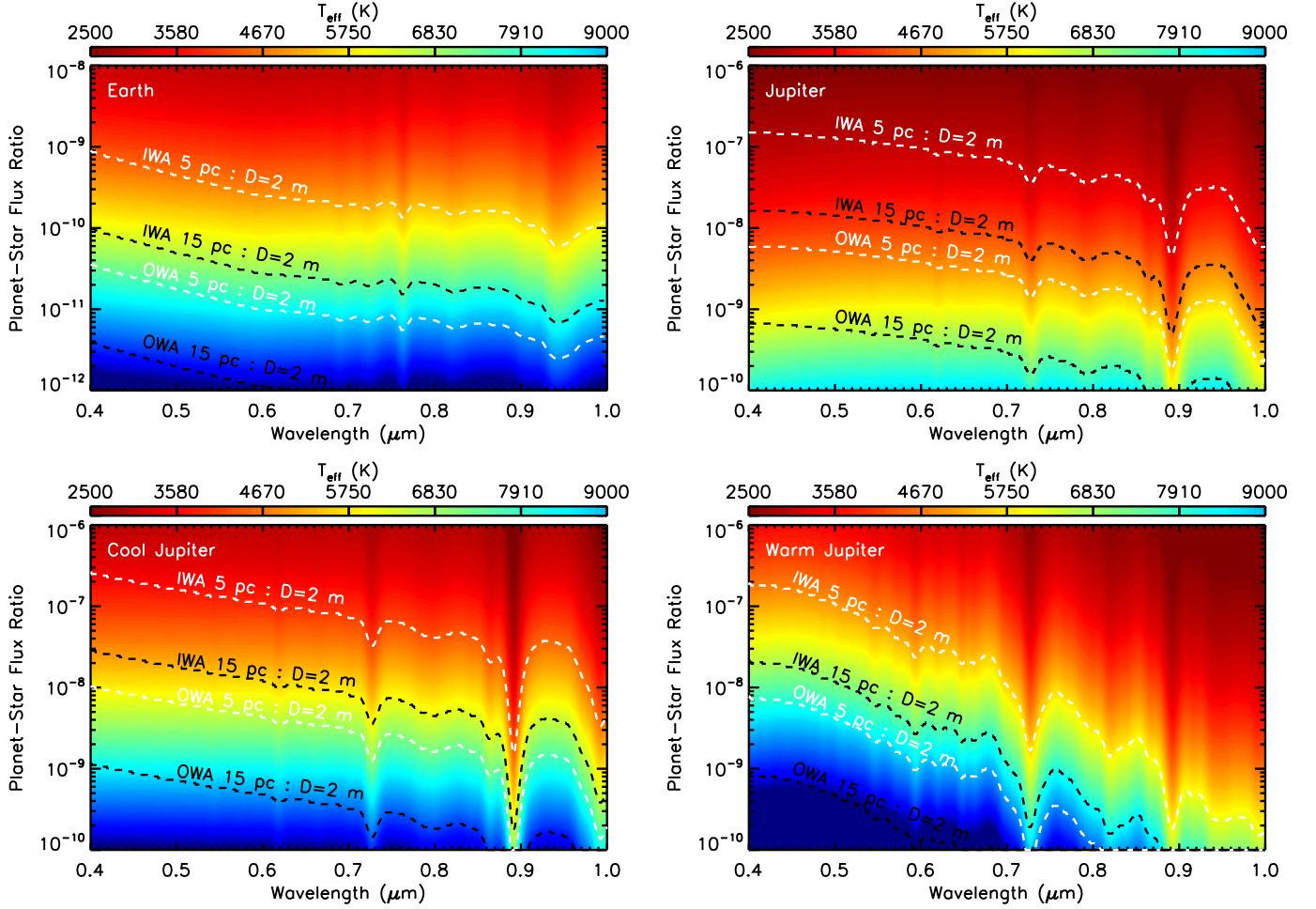


**Figure 5.** Contours of stellar effective temperature around which a certain planet type achieves a given planet–star flux ratio. Jupiter-sized cases are the same as in Figure 2, while the Earth case is as in Figure 4. Inner and outer working angle constraints are also shown and follow those in Figure 2. (A color version of this figure is available in the online journal.)

their influence on our ability to characterize a planet for key atmospheric constituents.

Figure 13 shows the integration time required to achieve  $S/N = 5$  in the bottom of the  $0.73 \mu\text{m}$  methane band as well as the integration time required to detect this band  $S/N_{\text{band}} = 5$  for our cool Jupiter model. Panels demonstrate sensitivity to exozodi levels and raw contrast performance at a fixed distance of 10 pc. For these studies, the coronagraph IWA prevents observations of this planet type around stars cooler than 5300 K. As the  $0.73 \mu\text{m}$  methane band is not particularly deep or wide in the cool Jupiter reflectance spectrum, integration times for band detection are longer than for detecting the bottom of the band. Nevertheless, even at poor raw contrast performance and/or larger ( $N_{\text{ex}} \gtrsim 10$ ) levels of exozodi, integration times for either band bottom or species detection are below 100 hr.

Figure 14 is similar to Figure 13, but for the cool Neptune model. Here we use the  $0.62 \mu\text{m}$  methane band, because, as mentioned earlier, the bottom of the  $0.73 \mu\text{m}$  band is at a contrast ratio of less than  $10^{-10}$ . We place the planet–star systems at a distance of 5 pc. Integration times for band detection are now shorter than for detecting the bottom of the band, as the  $0.62 \mu\text{m}$  methane band is deeper in the cool Neptune reflectance spectrum than the  $0.73 \mu\text{m}$  band in the cool Jupiter spectrum.

Finally, Figure 15 shows sensitivity tests for the integration times required to detect the  $0.76 \mu\text{m}$  oxygen A-band for  $1.5R_{\oplus}$  super-Earths. We place the planet–star systems at a distance of 3.7 pc, which is roughly the distance to  $\tau$  Ceti. We do not consider the  $0.94 \mu\text{m}$  water vapor band as Figure 12 shows that detecting this band at 3.7 pc would require nearly a  $10^4$  hr integration time. Also, we do not consider the integration time

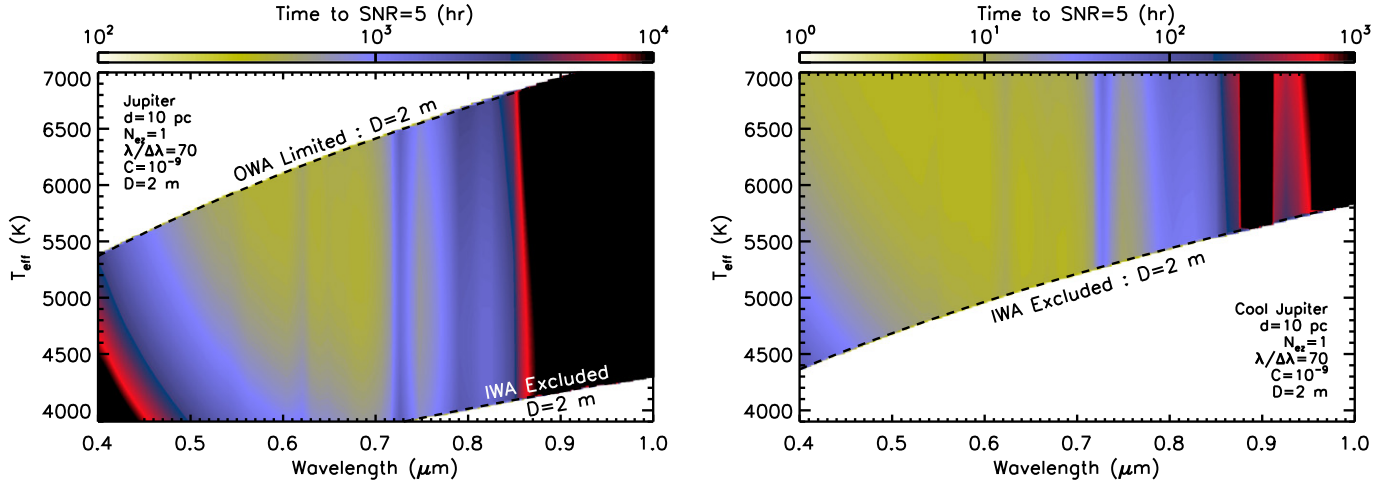


**Figure 6.** Contours of integration time required to achieve  $S/N = 5$  for a Jupiter twin (left) and a cool Jupiter (right) at 10 pc. These planet types are placed at the flux equivalent distance of main-sequence stars of different effective temperatures, as in Figure 2. Note the two different color-bar scales. Regions excluded/limited by a  $2\lambda/D$  and  $10\lambda/D$  inner and outer working angle (respectively) are demarcated by a dashed line.

(A color version of this figure is available in the online journal.)

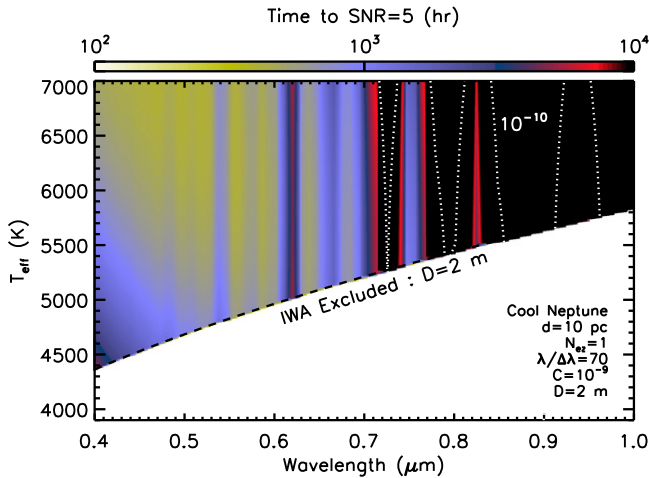


**Figure 7.** Same as Figure 6, but for a cool Neptune placed at the flux equivalent distance, as in Figure 3. Regions with planet-star flux ratios smaller than  $10^{-10}$  are above the labeled dotted line.

(A color version of this figure is available in the online journal.)

required to detect the bottom of the band as this is shorter than the time to detect the band.

### 3.5. Toward Large UV–Optical–Infrared Telescopes

Large UV-optical-infrared telescopes have been proposed as important tools for continuing NASA’s vision for exploring and characterizing exoplanets beyond the *James Webb Space Telescope* mission (Kouveliotou et al. 2014). The capabilities of such a 10 m class space-based telescope, if equipped with a coronagraph, can be investigated using the formalism outlined above. As an example, Figure 16 shows integration times to

$S/N = 5$  across a broad wavelength range, and sensitivity to exozodi levels for the  $0.76\ \mu\text{m}$  oxygen A-band for Earth twins, as would be the primary target of a LUVOIR mission. We have adopted an extended wavelength range ( $0.4\text{--}3\ \mu\text{m}$ ) and have assumed the distance to these systems is 10 pc. We have extended the OWA to a more generous  $20\lambda/D$  and use  $C = 10^{-10}$ , as could hopefully be achieved by such a distant-future mission. Also, we extend the IWA to  $3\lambda/D$ , as telescope stability for a 10 m class observatory would make achieving smaller IWAs very challenging. (Note that this larger IWA is outside the  $2\lambda/D$  “practical limit to small IWA coronagraphy,” determined by Mawet et al. 2014.) Finally, we assume that the visible and near-infrared wavelength ranges would be handled by two separate detectors, with respective pixel/lenslet sizes determined at  $0.4$  and  $1.0\ \mu\text{m}$ . For the near-infrared detector, we adopt a dark current, read noise, and quantum efficiency that are representative of HgCdTe detectors (Morgan & Siegler 2015). Specifically, we use  $D_{e-} = 10^{-3}\ \text{s}^{-1}$ ,  $R_{e-} = 1$ , and  $q = 0.85$ . The visible wavelength detector is the same as our baseline model, except we adopt a more optimistic dark current of  $D_{e-} = 10^{-4}\ \text{s}^{-1}$ .

For the adopted LUVOIR architecture and for Earth twins at 10 pc, most of the wavelength- $T_{\text{eff}}$  parameter space is dominated by noise from dark current, which is not influenced by telescope diameter. If not for the larger dark current rates of the near-infrared HgCdTe detector, exozodiacal light would be the dominant noise source at longer wavelengths, owing to its strong wavelength dependence ( $\propto \lambda^4 F_{s,\lambda}$ ). Note also that the wavelength-dependent IWA at  $3\lambda/D$  limits our ability to obtain a full spectrum through the near-infrared for all but the hottest stars. For Earth twins at 5 pc, the IWA restrictions are less strict (although the OWA can restrict observations at quadrature for

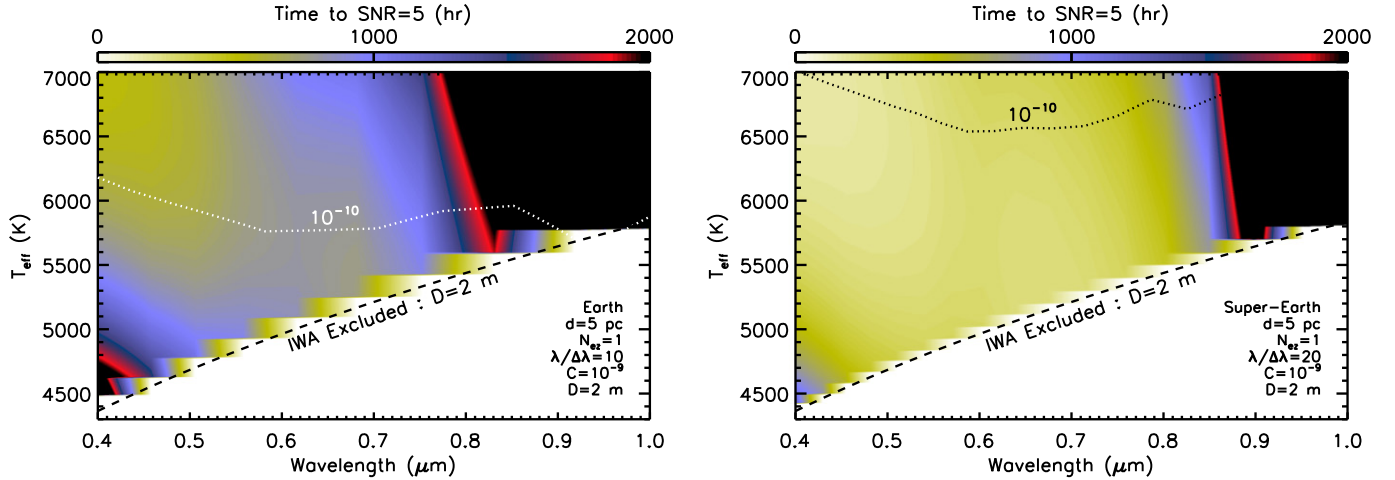


**Figure 8.** Same as Figure 6, but for an Earth twin (left) and a  $1.5 R_{\oplus}$  super-Earth (right) at 5 pc. Both are placed at Earth’s flux equivalent distance (as in Figure 4). To maintain reasonable integration times, higher-resolution spectra ( $\mathcal{R} = 70$ ) have been degraded to  $\mathcal{R} = 10$  and  $\mathcal{R} = 20$  for the Earth twins and super-Earths, respectively. Regions with planet–star flux ratios smaller than  $10^{-10}$  are above the labeled dotted line.

(A color version of this figure is available in the online journal.)

stars hotter than 5500 K), and leakage from the star can dominate over other noise sources at visible wavelengths for stars hotter than about 6000 K. This all assumes that the telescope system can be cooled to a sufficiently low temperature to minimize thermal noise contributions to observations in the near-infrared (i.e., below about 80 K). As an example of the capabilities of a LUVOIR mission, Figure 17 shows a simulated observation of an Earth twin orbiting a solar twin, assuming the system is at 10 pc and an integration time of 200 hr. Note that IWA constraints cut off the observations at the longest wavelengths.

#### 4. Discussion

Direct characterization of exoplanets in reflected light will require moving beyond V-band detections and will utilize a wide range of wavelengths. This added spectral dimension influences our understanding of spectrographic observations with coronagraph-equipped telescopes in a variety of ways. First, planet–star flux ratios are a strong function of wavelength, owing to the presence of gaseous and aerosol absorption/extinction features (e.g., Marley et al. 1999; Sudarsky et al. 2003; Burrows et al. 2004; Cahoy et al. 2010). Thus, while a coronagraph may provide a raw contrast, or achieve a contrast floor, that can detect certain planet types at continuum wavelengths, this performance may not permit adequate S/Ns in molecular absorption bands, thereby impeding characterization attempts.

Second, as coronagraphs have inner and outer working angles that depend on wavelength, the variety of planets accessible for observation will depend on distance from the Solar System. The interplay between planet–star flux ratio, wavelength, host star effective temperature, and inner and outer

working angle constraints are depicted for different planet types in Figures 2–4. These contour diagrams are extremely useful for understanding the types of observations that could be made by a given mission architecture and, to our knowledge, are the first of their kind. Additionally, these diagrams depict an important reality of exoplanet spectral characterization: wavelength-dependent instrument inner and/or outer working angles can cause portions of an exoplanetary spectrum to be unobservable, depending on the apparent planet–star separation at the time of observation.

Recall that we have defined a planet “type” based, in part, on insolation and size. Thus, Figures 2–4 show that a  $2\lambda/D$  IWA for a 2 m class telescope will strongly limit our ability to study warm Jupiters and Neptunes (at distances equivalent to 0.8 AU from the Sun) and Venus-like planets. Cool Jupiters and Neptunes (at distances equivalent to 2 AU from the Sun) are much more accessible. Interestingly, the presence of thick water clouds in the atmospheres of the cool Jupiters and Neptunes make these worlds very reflective compared to their warm counterparts (Sudarsky et al. 2000; Cahoy et al. 2010). Hence, the planet–star flux ratios in Figures 2 and 3 are broadly similar for these planet types, even though the insolation levels of the warm planet types is over six times larger.

For our baseline parameters, integration times for cool Jupiters are relatively short, even out to 10 pc (Figure 6). Detecting the bottom of the  $0.73 \mu\text{m}$  methane band, which could indicate different planet formation scenarios as it can distinguish between different amounts of heavy element enhancement (Cahoy et al. 2010), can be accomplished with a 10 hr integration time (or less) for distances as large as 7 pc and with 100 hr integration times out to 13 pc (Figure 9). Integration times required to detect the  $0.73 \mu\text{m}$  methane band



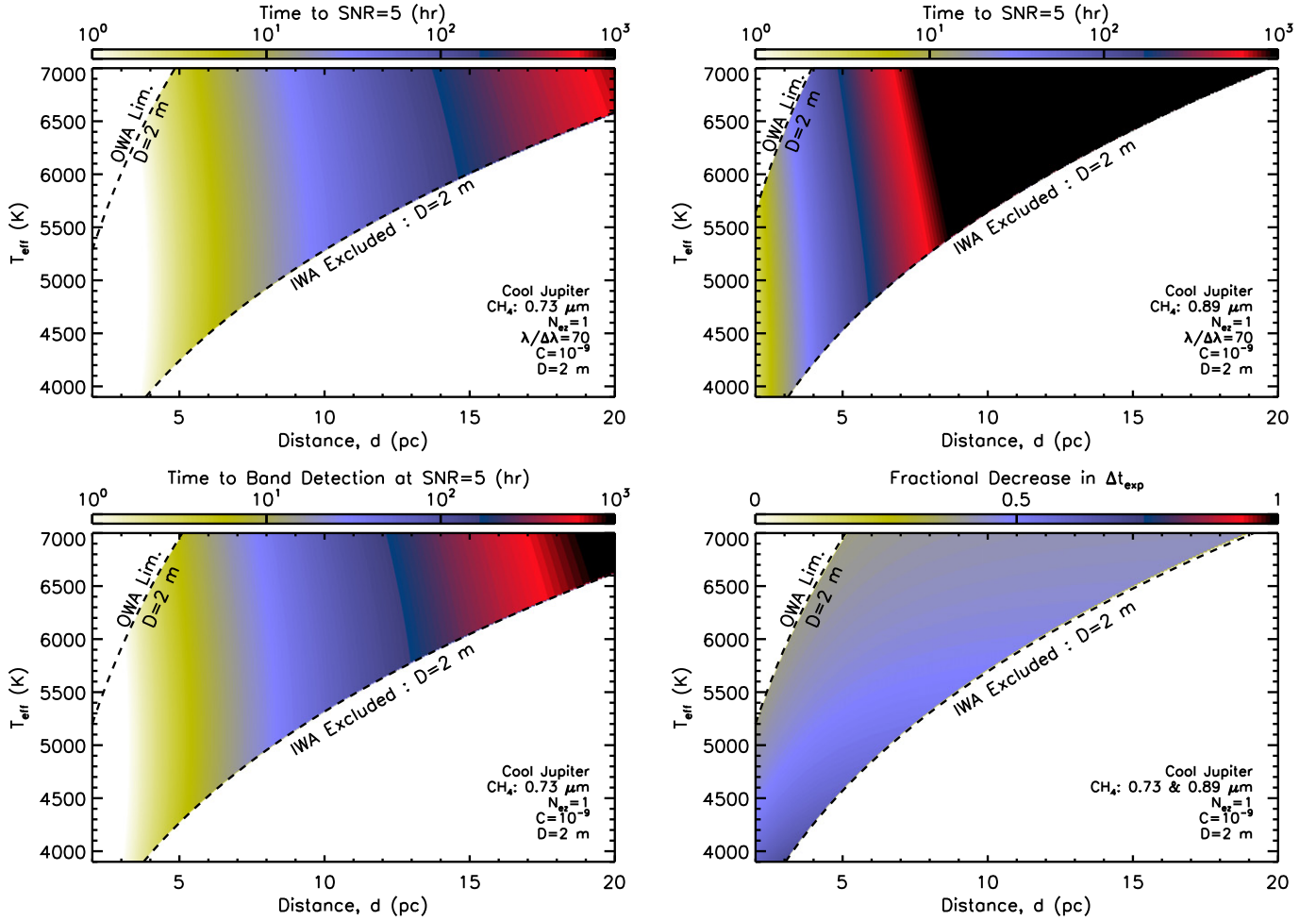


**Figure 9.** Contours of integration time required to achieve  $S/N = 5$  in the bottom of key absorption bands as well as contours of required integration time to detect a band at  $S/N_{\text{band}} = 5$  for cool Jupiters. We highlight the 0.73 and 0.89  $\mu\text{m}$  methane bands. The lower right plot shows how the band detection time decreases when both methane features are used. Regions excluded/limited by a  $2\lambda/D$  and  $10\lambda/D$  inner and outer working angle (respectively) are demarcated by a dashed line. (A color version of this figure is available in the online journal.)

are similar and could be decreased by about 50% by observing both the 0.73 and 0.89  $\mu\text{m}$  methane bands. Detecting the bottom of the 0.89  $\mu\text{m}$  band in less than 100 hr is limited to cool Jupiters at distances of 6 pc or less, where the overall longer integration times for detecting the bottom of this band are driven up by falling detector quantum efficiencies at these wavelengths. Finally, these integration times are largely insensitive to raw contrast performance and exozodi levels (Figure 13). Regarding the latter, dust clearing by giant planets will likely prevent large exozodi levels in the vicinity of a giant (e.g., Papaloizou et al. 2007), limiting the range of realistic values for  $N_{\text{ez}}$  in Figure 13.

Resolution 70 spectra at constant  $S/N$  for Jupiter twins are limited by long integration times in methane bands at long wavelengths, which can exceed 10<sup>3</sup> hr (Figure 6). Such long integration times are unrealistic (especially on a shared

resource like WFIRST-AFTA—the *Hubble* Deep Field used less than 200 hr of exposure time). Only for continuum wavelengths between about 0.5 and 0.8  $\mu\text{m}$  do integration times for  $S/N = 5$  spectra fall below 10<sup>3</sup> hr for a Jupiter twin at 10 pc. While integration times for Jupiter twins around closer (i.e., less than about 5 pc) stars would be much shorter, telescope OWA constraints would limit study of twins in these nearby systems to cool stars (i.e., roughly 4300 K or less for the orbit to be entirely within the OWA). Note, however, that the OWA constraint is less strict than the IWA constraint, as some fraction of the orbit, both toward gibbous and crescent phases, can occur inside the OWA, depending on orbit parameters and orientation (see, e.g., Greco & Burrows 2015).

For the cool Neptunes, a coronagraph contrast noise floor of 10<sup>-10</sup> would strongly limit observations at longer wavelengths

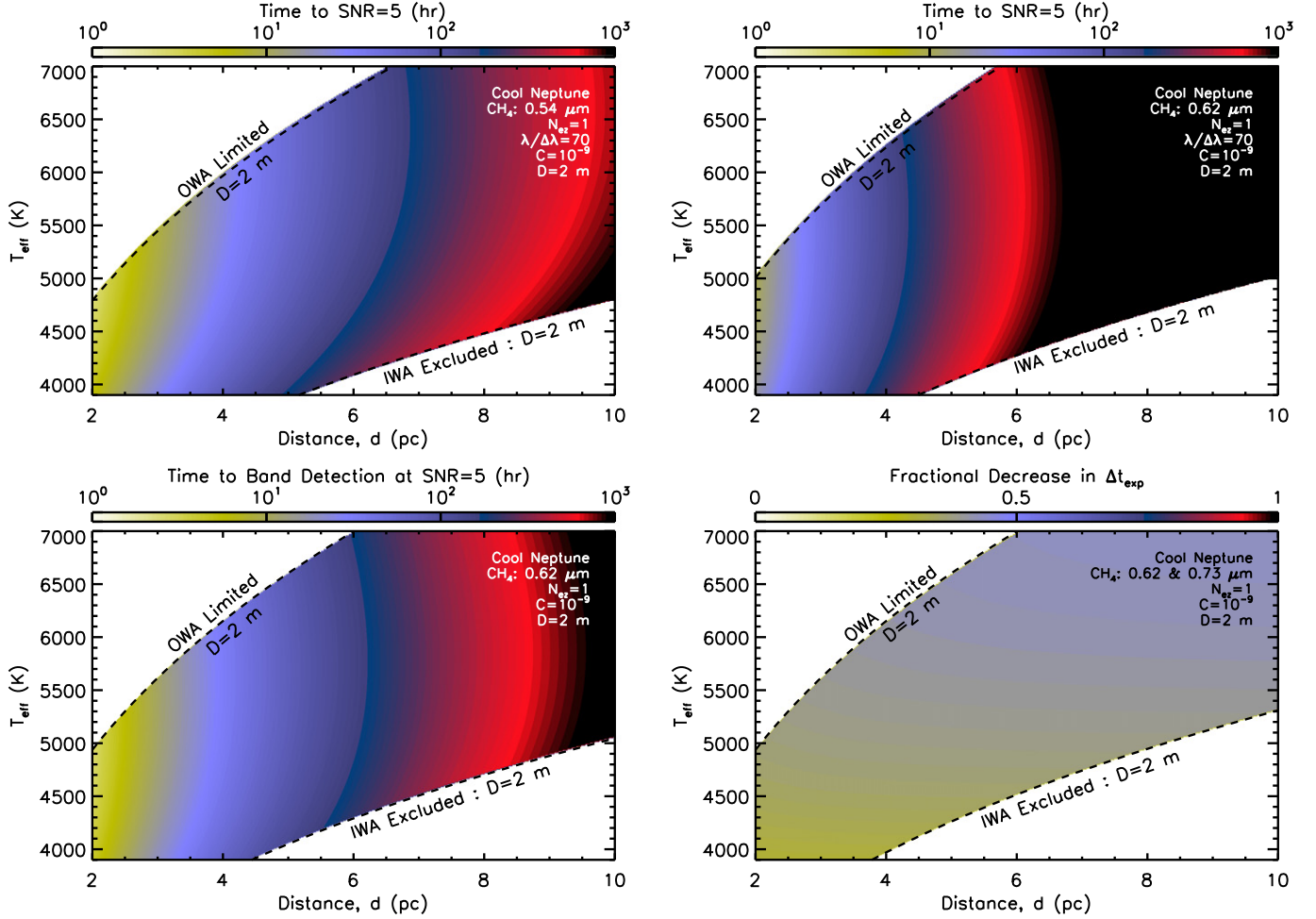


**Figure 10.** Similar to Figure 9, except now for cool Neptunes. Here, for detecting the bottom of features, we highlight the 0.54 and 0.62  $\mu\text{m}$  methane bands, as the longer wavelength bands have planet–star flux ratios of  $10^{-10}$  or smaller in their bases. For band detections, we use the 0.73  $\mu\text{m}$  methane band, as its depth leads to shorter required integration times than bands at shorter wavelengths. The lower right plot shows how the band detection time decreases when both the 0.62 and 0.73  $\mu\text{m}$  methane features are used.

(A color version of this figure is available in the online journal.)

(Figure 7), although detecting the 0.62  $\mu\text{m}$  methane band with integration times below 100 hr can be done out to distances of about 5 pc (Figure 10). As this band is relatively deep in the reflectance spectrum of cool Neptunes, integration times for detecting the bottom of the 0.62  $\mu\text{m}$  band are longer, remaining below 100 hr only out to 3–4 pc. The 0.54  $\mu\text{m}$  methane band is shallower, so detecting its bottom can be done with integration times comparable to the band detection times for the 0.62  $\mu\text{m}$  band.

Inner working angle constraints strongly limit the ability of a 2 m class telescope to study Earths and super-Earths at 1 AU flux equivalent distances from their host stars. Covering the entire 0.4–1  $\mu\text{m}$  spectral range at a distance of 5 pc (or more) requires solar twins (or hotter). For Earth twins, this implies planet–star flux ratios of  $10^{-10}$ – $10^{-11}$ , which could be improved by a factor of  $(R_p/R_\oplus)^2$  for super-Earths (assuming

similar reflectivity). Additionally, maintaining integration times below even  $10^3$  hr at continuum wavelengths for these worlds at 5 pc would require degrading spectra to  $\mathcal{R} = 10$ –20 to achieve  $S/N = 5$  (Figure 8), notably ruling out detection of the 0.76  $\mu\text{m}$  oxygen A-band (Brandt & Spiegel 2014). Such long integration times may be an unrealistic price to pay for characterizing potentially habitable worlds. Additionally, a  $2\lambda/D$  coronagraph IWA could interfere with our ability to detect the 0.94  $\mu\text{m}$  water vapor band, a key indicator of habitability, for 5 pc Earths and super-Earths around Sun-like stars and cooler. These IWA constraints could be alleviated by investigating worlds at the outer edge of the habitable zone (Kasting et al. 1993; Kopparapu et al. 2013), but the low incident flux on these worlds pushes integration to times  $\gtrsim 10^3$  hr (assuming an Earth-like size and reflectivity), even at  $\mathcal{R} = 10$ .

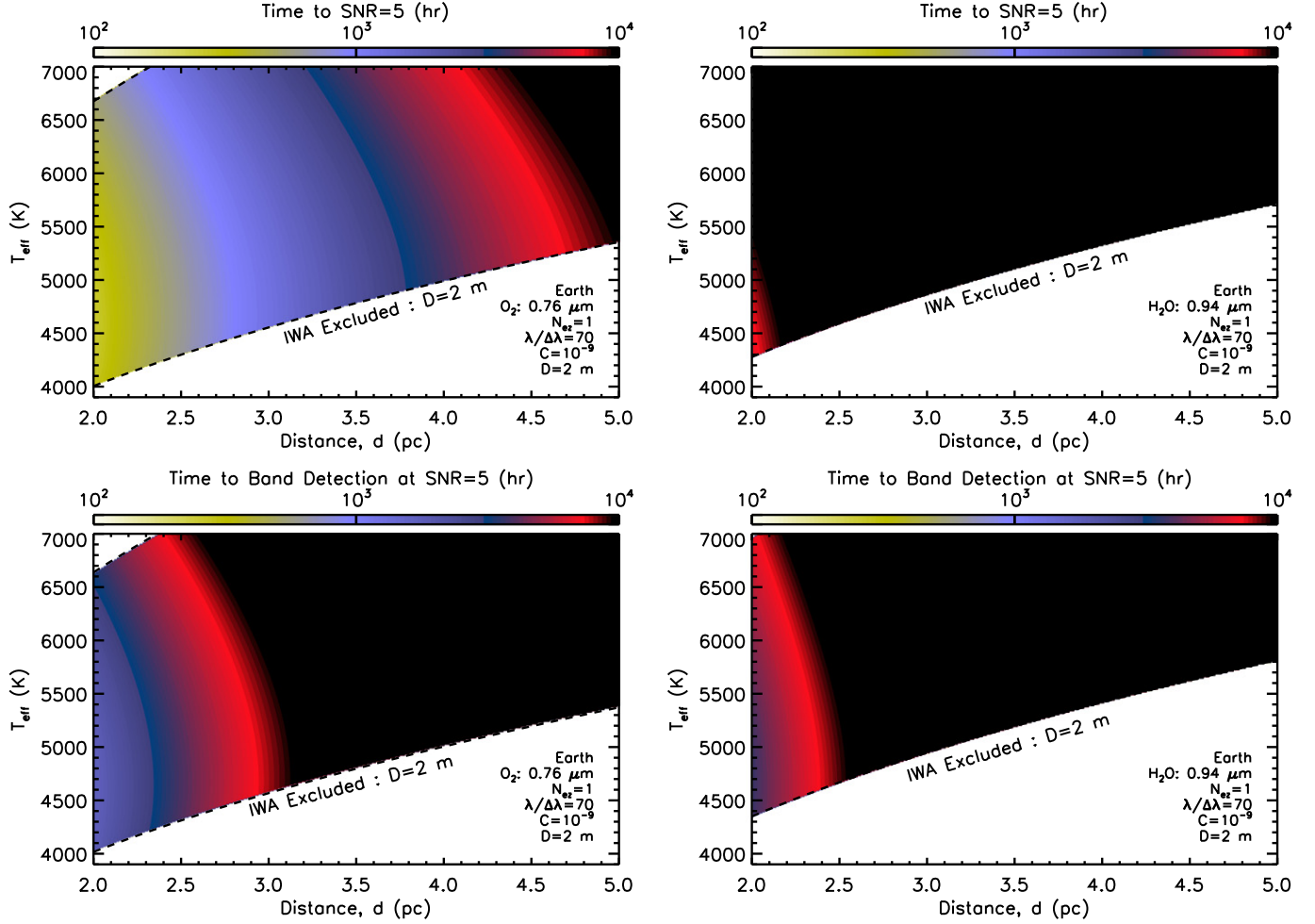


**Figure 11.** Similar to Figure 9, except now for Earth twins. Here, we focus on the  $0.76\ \mu\text{m}$  A-band of molecular oxygen and the  $0.94\ \mu\text{m}$  water vapor band. (A color version of this figure is available in the online journal.)

Shorter integration times and more favorable contrast ratios argue for super-Earths as being more attractive targets than Earth-sized worlds. Even for these worlds, though, detecting the oxygen A-band with integration times less than  $10^3$  hr requires targets to be nearer than about 3 pc (Figure 13). Only a few stars meet the distance and effective temperature requirements ( $\alpha$  Centauri A and B,  $\epsilon$  Eridani), and most of these stars are in multi-star systems. Detecting the  $0.94\ \mu\text{m}$  water vapor band in super-Earth spectra with integration times below  $10^3$  hr will be extremely challenging, if not impossible, owing in large part to extremely low detector quantum efficiencies at these wavelengths. This outlook could be improved by using detectors with better quantum efficiency at red visible wavelengths, although these detectors tend to have larger dark currents, which might diminish any possible improvements.

While our results show that characterizing Earth twins with a 2 m class, coronagraph-equipped telescope will be unlikely, 10 m class LUVOIR telescopes show much more promising

results (Figure 16). Such a mission could achieve  $\mathcal{R} = 70$  visible wavelength spectra at  $S/N = 5$  for Earth twins at a characteristic distance of 10 pc for integration times of the order of 100 hr. Falling stellar spectra and strong water vapor absorption drive up integration times at near-infrared wavelengths. Additionally, falling CCD quantum efficiency will drive up required integration times for species and band bottom detection at red visible wavelengths, especially for the  $0.94\ \mu\text{m}$  water vapor band. Using the near-infrared HgCdTe detector at these wavelengths can improve required integration times by an order of magnitude, even when accounting for the larger dark current and read noise in these detectors. Finally, note that telescope IWA constraints can prevent observations of large parts of the near-infrared wavelength range for Earth twins orbiting Sun-like stars at 10 pc, and exozodi levels larger than  $N_{\text{ez}} = 10$  begin to rapidly drive up integration times.

Moving beyond requisite integration times and sensitivities, several of our assumptions about our instrumental,

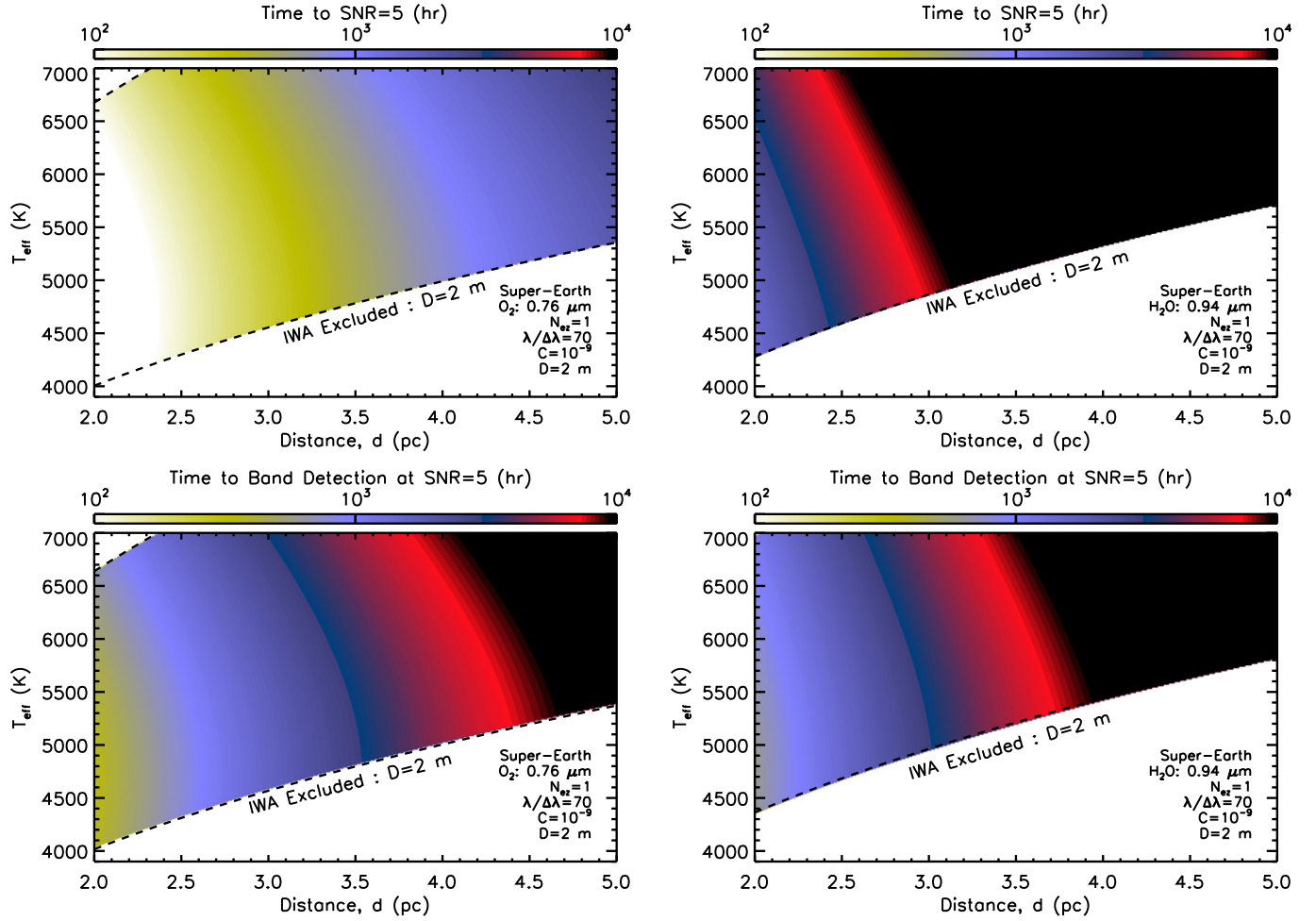


**Figure 12.** Same as Figure 11, except for  $1.5R_{\oplus}$  super-Earths.  
(A color version of this figure is available in the online journal.)

astrophysical, and planetary parameters warrant further discussion. Most notably, current experimental coronagraphs designed to achieve raw contrasts suitable for exoplanet characterization typically operate only over a  $\sim 20\%$  bandpass (e.g., Trauger et al. 2013), which is limited by chromatic effects within the wavefront control system (although progress is being made on some aspects of this problem; e.g., Newman et al. 2015). Thus, if only a single coronagraph is used, observing over the full  $0.4\text{--}1.0\ \mu\text{m}$  range used in this work would require 4–5 separate integrations, thereby driving up overall characterization time. This feature of coronagraphs is not entirely negative, as integration times in different bandpasses could be tailored to prevent achieving unnecessarily large S/Ns in bright spectral regions. Also, while we include stellar leakage from the coronagraph, we did not consider how systematic errors from speckle subtraction might impact performance and increase required integration times, all of which would depend on telescope stability, the capabilities

of the coronagraph wavefront control system, and how well speckles can be modeled (Krist et al. 2008).

Regarding astrophysical assumptions, recall that our noise models assumed that the star–planet systems were isolated in the instrument field of view. In reality, stellar companions (which are common; see Duchêne & Kraus 2013) and background objects will contribute light to the observations, possibly within the planetary PSF. Stray light from a companion could impact the systematic contrast noise floor and/or the raw contrast performance. While simplistic for companion star scenarios, our sensitivity studies to raw contrast performance ( $C$ ) provide an estimate for how integration times would change if a companion were to increase the contrast background. Also, we assume smoothly varying exozodiacal structure that only depends on distance from the host star. Real exozodiacal disks will have more complex structure, such as clumps and bands, and studies of such structure would be a major science driver of a space-based coronagraph mission.



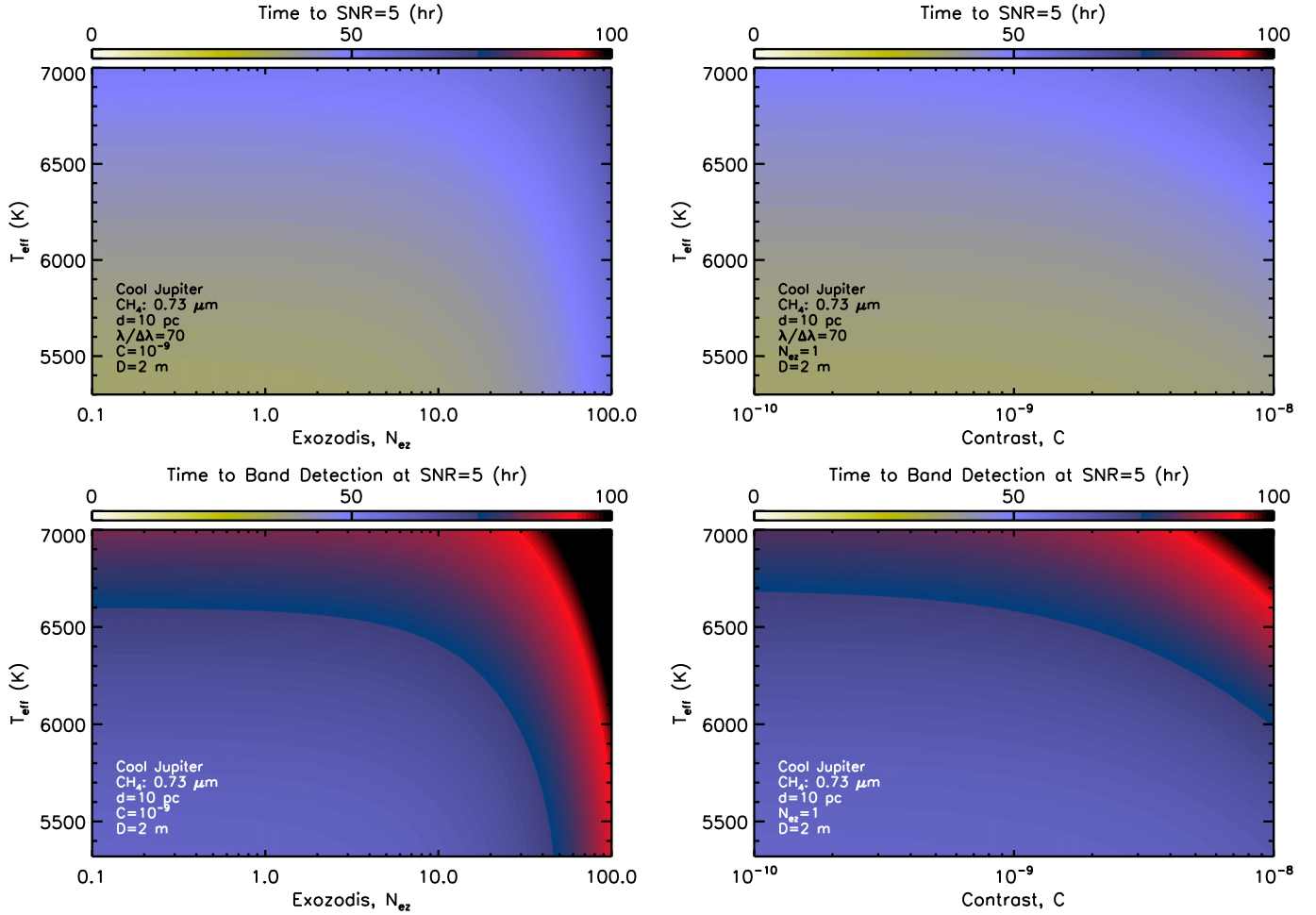


**Figure 13.** Contours of integration time required to achieve  $S/N = 5$  in the bottom of the  $0.73 \mu\text{m}$  methane band (top) or to detect this band at  $S/N_{\text{band}} = 5$  (bottom) for a cool Jupiter at a distance of 10 pc for various levels of exozodis and raw contrast. Note that the IWA limits the range of  $T_{\text{eff}}$  that can be investigated (as the wavelength and distance are fixed).

(A color version of this figure is available in the online journal.)

While we have presented a range of planet models and types, the true diversity of exoplanets will be much greater. Additionally, some of our planet types (the warm and cool Jupiters and Neptunes) are based on models that do not include atmospheric photochemistry. For the Solar System gas and ice giants, this chemistry leads to haze formation, which causes lower albedos at blue wavelengths (Karkoschka 1994). Thus, we are likely underestimating integration times for these worlds at the shortest wavelengths. Also, our placement of planet types at flux equivalent distances attempts, to first order, to maintain self-consistent atmospheric and cloud structures for these worlds. This treatment does not account for the shift of cooler stellar spectral energy distributions to longer wavelengths, where planets tend to be more absorbing (Marley et al. 1999). So, our planet types around cooler stars would be absorbing more stellar flux, implying that an “absorbed flux” equivalent

distance is further from the host star than our incident bolometric flux equivalent distance.

## 5. Conclusions

Space-based 2 m class exoplanet characterization missions have the potential to provide spectra at moderate to high  $S/N$ s (i.e., 5 or better) for a variety of planets, some of which have no analog in our Solar System. We find that:

1. For cool Jupiters (i.e., Jupiters at 2 AU flux equivalent distance from the Sun), methane can be detected with integration times shorter than 100 hr out to a distance of 13 pc, and with integration times less than 10 hr at 5 pc.
2. Spectra of cool Neptunes at 10 pc will be challenging (i.e., integration times approaching or exceeding  $10^3$  hr),

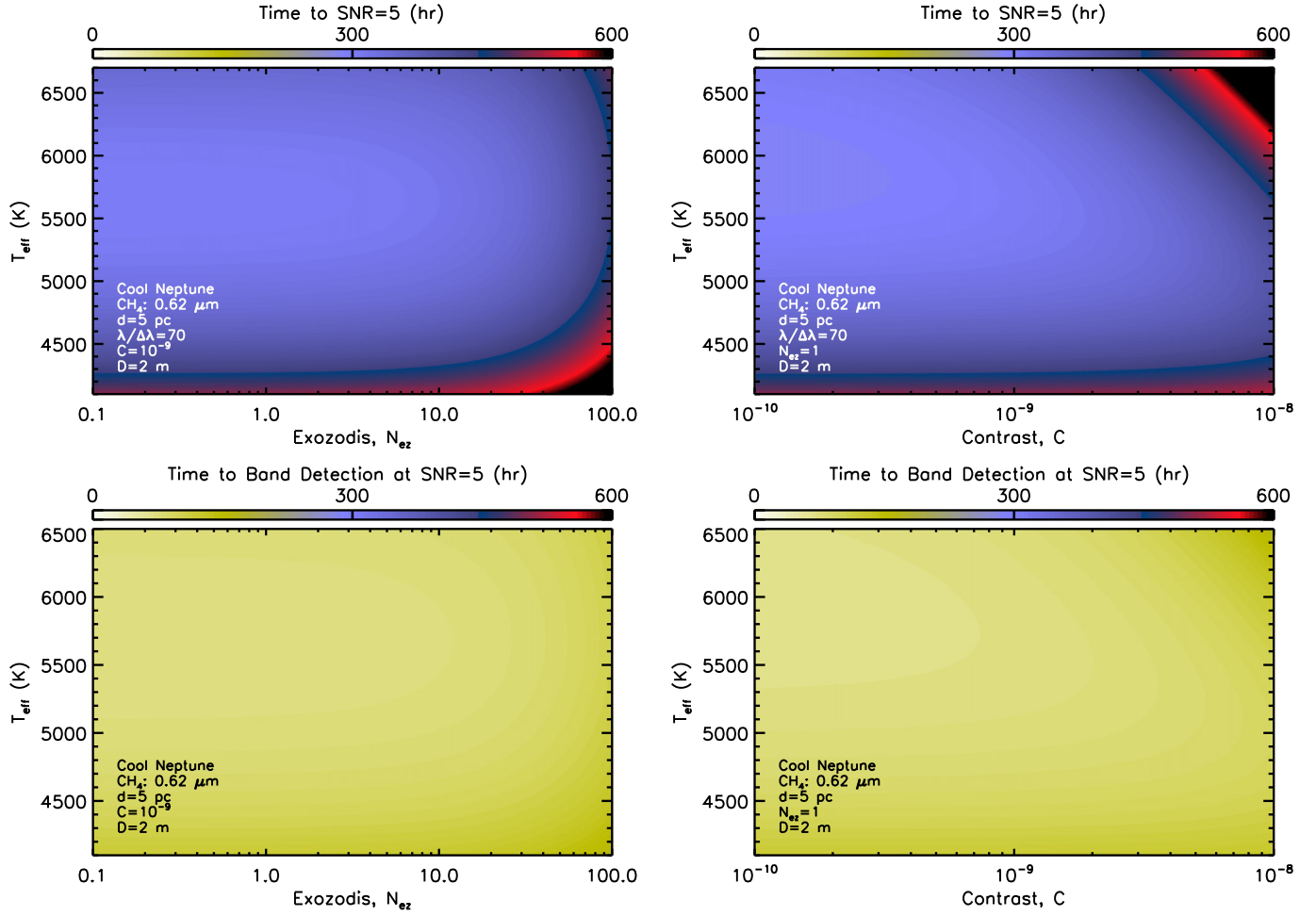


**Figure 14.** Similar to Figure 13 except for cool Neptunes at a distance of 5 pc. Here, the  $0.62 \mu\text{m}$  methane band is used for the feature bottom values, while the  $0.73 \mu\text{m}$  methane band is used for the band detection values.

(A color version of this figure is available in the online journal.)

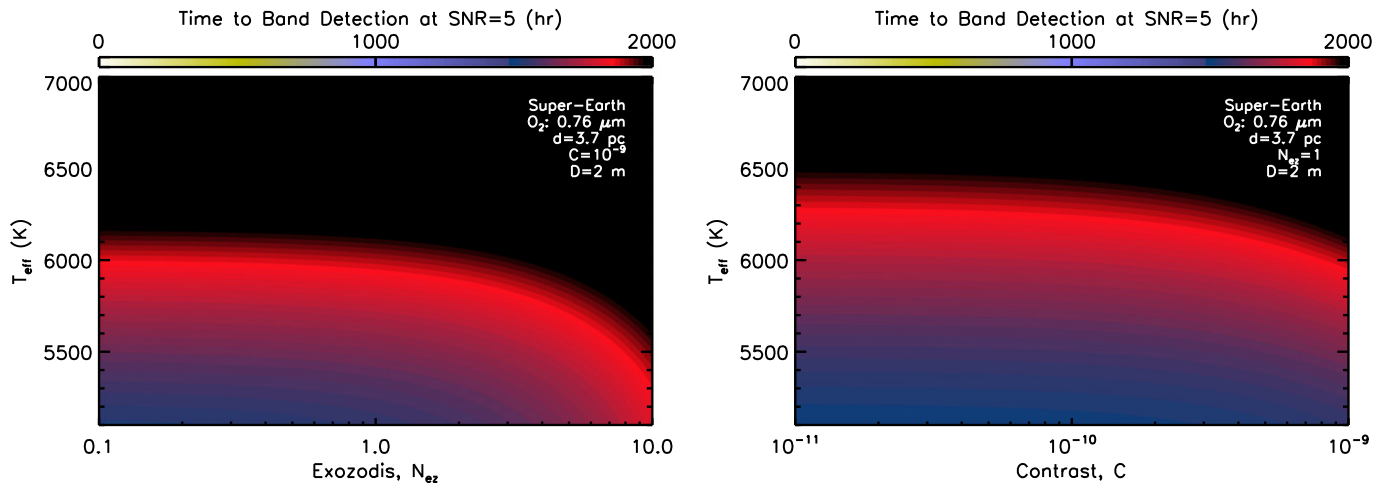


**Figure 15.** Similar to Figure 13, except for the required band detection time for the  $0.76 \mu\text{m}$  A-band of molecular oxygen for super-Earths at 3.7 pc.

(A color version of this figure is available in the online journal.)

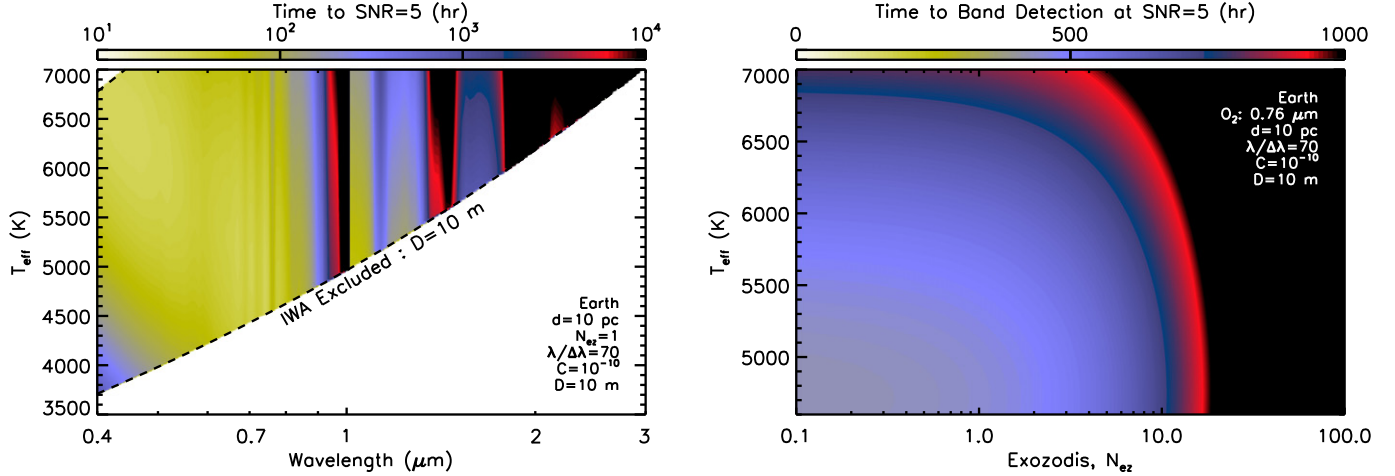


**Figure 16.** Results for a 10 m class space-based telescope and coronagraph, capable of  $10^{-10}$  raw contrast between an IWA of  $3\lambda/D$  and an OWA of  $20\lambda/D$ . For Earth twins around stars of different effective temperatures, panels show the integration times to achieve  $S/N = 5$  and sensitivity to exozodi levels for integration times in the A-band of molecular oxygen at  $0.76 \mu\text{m}$ .

(A color version of this figure is available in the online journal.)

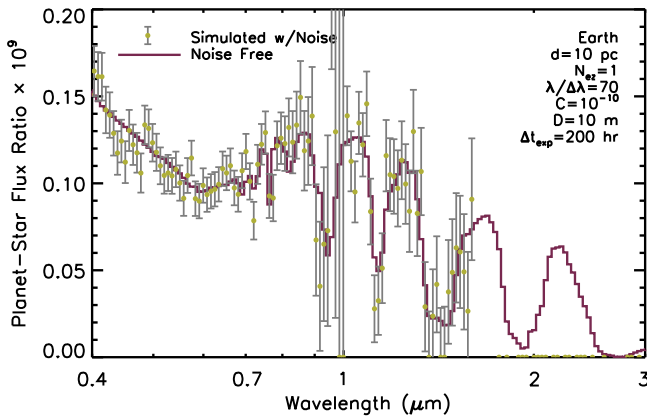


**Figure 17.** Simulated spectral observation of an Earth twin around a solar twin at 10 pc for a LUVOIR mission assuming a 200 hr integration. The dark red line is a noise-free spectrum, while the yellow points are a simulated spectrum (with  $1\sigma$  error bars in gray).

(A color version of this figure is available in the online journal.)

although methane could be detected in the spectra of these worlds with integration times below 100 hr out to a distance of 5 pc.

3. Earth twins are unlikely to be characterized, owing to long integration times and planet–star flux ratios smaller than  $10^{-10}$  for a wide range of stellar effective temperatures.
4. Super-Earths could be studied with low-resolution spectra and integration times below  $10^3$  hr to a distance of 5 pc, but detecting features in higher-resolution spectra will be limited to worlds around a small handful of stars within 3 pc of the Sun.

5. Falling CCD quantum efficiency at red visible wavelengths strongly limits observations of the  $0.89 \mu\text{m}$  methane band and the  $0.94 \mu\text{m}$  water vapor band.

We note that the majority of the modeled observations of planet types presented here have  $\Delta t_{\text{exp}} \propto c_D/c_p^2$  (to achieve a given  $S/N$ ). Thus, major gains in driving down requisite integration times could be made by striving for larger instrument throughputs, better detector quantum efficiencies, and by using devices with low dark current (although achieving lower dark currents in modern detectors can lead to tradeoffs with other detector properties; Harding et al. 2015). Observational investigations will not have control over planetary properties, but we do have control over instrument performance requirements.

T.R. gratefully acknowledges support from an appointment to the NASA Postdoctoral Program at NASA Ames Research Center, administered by Oak Ridge Affiliated Universities, and from NASA through the Sagan Fellowship Program executed by the NASA Exoplanet Science Institute. M.M. acknowledges support of the NASA Planetary Atmospheres and Origins programs. K.S. thanks NASA support for the *Exo-C mission* study through the Exoplanet Exploration Program and the Goddard Space Flight Center. All authors thank M. Line and C. Stark for constructive feedback. The results reported herein benefitted from collaborations and/or information exchange within NASA’s Nexus for Exoplanet System Science (NExSS) research coordination network sponsored by NASA’s Science Mission Directorate. Results related to LUVOIR telescopes benefitted from discussions with S. Domagal-Goldman and G. Arney, as part of collaborative work done within the NASA Astrobiology Institute’s Virtual Planetary Laboratory,

supported by NASA under Cooperative Agreement No. NNA13AA93A.

## Appendix: Noise Model Expressions

This appendix contains a brief discussion of our models of the planet count rate and count rates from key noise sources.

### A.1. Planet Count Rate

The planetary signal is the incident stellar host spectrum, weighted by a wavelength- and phase-dependent planetary reflectance, and passed through the optics of a distant telescope. We assume that the host star has radius  $R_s$  and a spectrum of a blackbody,  $B_\lambda(T_{\text{eff}})$ , where  $T_{\text{eff}}$  is the stellar effective temperature. Thus, the specific flux density at a distance  $d$  from the stellar host is

$$F_{s,\lambda}(d) = \pi B_\lambda(T_{\text{eff}}) \left( \frac{R_s}{d} \right)^2. \quad (9)$$

Note that non-blackbody stellar spectra, either from observations or models, can be used for  $F_{s,\lambda}(d)$ —we simply adopt blackbody spectra for efficiency, allowing us to rapidly model large swaths of parameter space. If the planetary target has radius  $R_p$ , orbits its host at a distance  $r$ , is observed at phase angle (i.e., star–planet–observer angle)  $\alpha$ , and has a wavelength-dependent geometric albedo  $A$ , then the specific flux density at a distance  $d$  from the planet is

$$\begin{aligned} F_{p,\lambda}(d) &= A\Phi(\alpha)F_{s,\lambda}(r) \left( \frac{R_p}{d} \right)^2 \\ &= \pi A\Phi(\alpha)B_\lambda(T_{\text{eff}}) \left( \frac{R_s}{r} \right)^2 \left( \frac{R_p}{d} \right)^2, \end{aligned} \quad (10)$$

where  $\Phi(\alpha)$  is the planetary phase function, which is generally a function of wavelength. Thus, the wavelength-dependent planet–star flux ratio is

$$\frac{F_{p,\lambda}}{F_{s,\lambda}} = A\Phi(\alpha) \left( \frac{R_p}{r} \right)^2, \quad (11)$$

which, of course, is only a function of the product of the geometric albedo and phase function (i.e., the phase-dependent planetary reflectivity), and the ratio of the planetary radius to the orbital separation.

At the telescope, a distance  $d$  from the star–planet system, the planetary flux is passed through the optical components, with total throughput  $\mathcal{T}$  (which can, in general, be wavelength-dependent) and spectral bandwidth  $\Delta\lambda$ , and converted into counts on the detector with quantum efficiency  $q$  (in dimensionless units of counts per photon). Thus, the planet count rate is given by

$$c_p = \pi q f_{\text{pa}} \mathcal{T} \frac{\lambda}{hc} F_{p,\lambda}(d) \Delta\lambda \left( \frac{D}{2} \right)^2, \quad (12)$$

which has dimensions of counts per unit time. Here,  $h$  is the Planck constant,  $c$  is the speed of light, and  $f_{\text{pa}}$  is a factor of order unity (computed using  $X$ , the photometric aperture length) that describes the fraction of light from the planet that falls within the photometric aperture. Inserting Equation (10) and rearranging, we have

$$c_p = q f_{\text{pa}} \mathcal{T} A \Phi(\alpha) B_\lambda(T_{\text{eff}}) \Delta\lambda \frac{\lambda}{hc} \left( \frac{\pi D R_s R_p}{2rd} \right)^2. \quad (13)$$

Furthermore, for a spectrometer with constant resolution,  $\mathcal{R} = \lambda/\Delta\lambda$ , we can express the planet count rate as

$$c_p = q f_{\text{pa}} \mathcal{T} A \Phi(\alpha) B_\lambda(T_{\text{eff}}) \frac{\lambda^2}{hc \mathcal{R}} \left( \frac{\pi D R_s R_p}{2rd} \right)^2. \quad (14)$$

### A.2. Zodiacal and Exozodiacal Light

Local zodiacal light is known to be a function of ecliptic latitude and longitude (Levasseur-Regourd & Dumont 1980), although Stark et al. (2014) demonstrated that a constant V-band surface brightness of  $M_{z,V} = 23$  mag arcsec $^{-2}$  was a reasonably accurate representation. Thus, we take the wavelength-dependent zodiacal light count rate to be given by

$$c_z = \pi q \mathcal{T} \Omega \Delta\lambda \frac{\lambda}{hc} \left( \frac{D}{2} \right)^2 \frac{F_{\odot,\lambda}(1 \text{ AU})}{F_{\odot,V}(1 \text{ AU})} F_{0,V} 10^{-M_{z,V}/2.5}, \quad (15)$$

where  $F_{\odot,\lambda}$  is the wavelength-dependent specific solar flux density,  $F_{\odot,V}$  is the solar flux density in the V-band,  $\Omega$  is the photometry aperture area (with dimensions of arcseconds $^2$ ), and  $F_{0,V}$  is the standard zero-magnitude V-band specific flux density ( $F_{0,V} = 3.6 \times 10^{-8} \text{ W m}^{-2} \mu\text{m}^{-1}$ ). We use a square aperture with width  $X\lambda/D$  along an edge, such that  $\Omega = (X\lambda/D)^2$ , to most accurately represent a square grid of pixels (or spaxels) that would be used to isolate the planet. Note that the ratio  $F_{\odot,\lambda}/F_{\odot,V}$  in Equation (15) forces the color of the zodiacal light spectrum to match that of the Sun, which is a reasonable approximation, especially at large elongation angles from the Sun (Leinert et al. 1981). Inserting  $\Omega$ , and assuming constant spectral resolution, we have

$$c_z = \pi q \mathcal{T} X^2 \frac{\lambda^4}{4hc \mathcal{R}} \frac{F_{\odot,\lambda}(1 \text{ AU})}{F_{\odot,V}(1 \text{ AU})} F_{0,V} 10^{-M_{z,V}/2.5}, \quad (16)$$

which is a strong function of wavelength.

Following Stark et al. (2014), we define a “zodi” as the surface brightness of an exozodiacal disk at 1 AU from a solar twin, which we label  $M_{\text{ez},V}$ . Then the wavelength-dependent exozodiacal light count rate is given by

$$\begin{aligned} c_{\text{ez}} &= \pi q \mathcal{T} \Omega \Delta\lambda \frac{\lambda}{hc} \left( \frac{D}{2} \right)^2 \left( \frac{1 \text{ AU}}{r} \right)^2 \frac{F_{s,\lambda}(1 \text{ AU})}{F_{s,V}(1 \text{ AU})} \\ &\times \frac{F_{s,V}(1 \text{ AU})}{F_{\odot,V}(1 \text{ AU})} N_{\text{ez}} F_{0,V} 10^{-M_{\text{ez},V}/2.5}, \end{aligned} \quad (17)$$



where  $N_{\text{ez}}$  is the number of exozodis in the disk. Note that the  $F_{\text{s},V}/F_{\odot,V}$  term ensures that exozodiacal light surface brightness scales with the intrinsic stellar brightness (at fixed orbital distance), and the  $(1 \text{ AU}/r)^2$  term causes the disk surface brightness to decrease with increasing orbital separation according to the  $1/r^2$  law. Again, inserting  $\Omega$ , and assuming constant spectral resolution, we have

$$c_{\text{ez}} = \pi q T X^2 \frac{\lambda^4}{4hc\mathcal{R}} \left( \frac{1 \text{ AU}}{r} \right)^2 \frac{F_{\text{s},\lambda}(1 \text{ AU})}{F_{\text{s},V}(1 \text{ AU})} \times \frac{F_{\text{s},V}(1 \text{ AU})}{F_{\odot,V}(1 \text{ AU})} N_{\text{ez}} F_{0,V} 10^{-M_{\text{ez},V}/2.5}. \quad (18)$$

For a discussion of the variety of different exozodiacal light treatments and exozodi definitions adopted throughout the literature, see Roberge et al. (2012). Note that while the zodiacal and exozodiacal light count rates are independent of telescope diameter, the ratio of the planetary signal to the zodiacal and exozodiacal light signals will depend on telescope size [ $c_p/(c_z + c_{\text{ez}}) \propto D^2$ ].

### A.3. Leakage, Dark Counts, and Read Noise

We consider several other key sources of noise. Stellar light leaked through the coronagraph (“leakage”) can contribute a large number of noise counts as the host star is many orders of magnitude brighter than the target planet. The leakage count rate is determined from the stellar photon flux passed through the observing system, diminished by  $C$  (the coronagraph design raw contrast), and is given by

$$c_{\text{lk}} = \pi q T C \Delta \lambda F_{\text{s},\lambda}(d) \frac{\lambda}{hc} \left( \frac{D}{2} \right)^2 = q T C B_{\lambda}(T_{\text{eff}}) \frac{\lambda^2}{hc\mathcal{R}} \left( \frac{\pi D R_s}{2d} \right)^2, \quad (19)$$

where the final step assumes constant spectral resolution. Detections are possible for sources fainter than the raw contrast, but coronagraphs will have systematic noise floors that limit how far below the raw contrast observations can go. The noise floor limit is due to residuals in the subtracted stellar PSF and is typically a factor of 10 below the raw contrast. This limit is important to keep in mind when discussing small, low-albedo, and/or large separation planetary companions.

For a given dark current  $D_{\text{e}^-}$ , in counts per pixel per unit time, the dark count rate is

$$c_{\text{D}} = D_{\text{e}^-} N_{\text{pix}}, \quad (20)$$

where  $N_{\text{pix}}$  is the number of detector pixels contributing to the spectral element. For imaging, the contributing pixels are those that fall within the aperture ( $\Omega$ ), so that, if a pixel has an

angular diameter  $\theta_{\text{pix}}$ , then

$$N_{\text{pix},i} = \frac{4\Omega}{\pi\theta_{\text{pix}}^2}, \quad (21)$$

where the subscript “i” has been introduced for “imaging.” If the pixel diameter is determined by the diffraction limit at some wavelength  $\lambda_0$ , giving  $\theta_{\text{pix}} \simeq \lambda_0/2D$ , then the number of contributing pixels is simply

$$N_{\text{pix},i} = \frac{16}{\pi} \left( \frac{X\lambda}{\lambda_0} \right)^2. \quad (22)$$

Determining the number of contributing pixels for a spectrometer is more complicated. For an integral field spectrometer, angularly resolved spectroscopic observations are obtained by placing a grid of small lenses (called “lenslets”) in the focal plane, spectrally dispersing the light from each lenslet, and recording the resulting spectra at the detector. For this setup, the number of contributing pixels is

$$N_{\text{pix},s} = n_{\text{pix}} \Delta \lambda \frac{4\Omega}{\pi\theta_{\text{lens}}^2}, \quad (23)$$

where “s” is for “spectroscopy,”  $n_{\text{pix}}$  is the number of pixels per unit wavelength designed for each lenslet spectrum, and  $\theta_{\text{lens}}$  is the angular diameter of an individual lenslet (so that  $4\Omega/\pi\theta_{\text{lens}}^2$  is the number of lenslets over which the aperture is distributed). For a spectrum sampled at two pixels per spectral resolution element and spread over  $\Delta N_{\text{hpix}}$  pixels in the horizontal/spatial dimension, we have

$$n_{\text{pix}} = \Delta N_{\text{hpix}} \frac{2\mathcal{R}}{\lambda} = \frac{2\Delta N_{\text{hpix}}}{\Delta \lambda}, \quad (24)$$

which gives

$$N_{\text{pix},s} = 8\Delta N_{\text{hpix}} \frac{\Omega}{\pi\theta_{\text{lens}}^2}. \quad (25)$$

Again, if the lenslets are sized to yield the diffraction limit at some reference wavelength, then we would have

$$N_{\text{pix},s} = \Delta N_{\text{hpix}} \frac{32}{\pi} \left( \frac{X\lambda}{\lambda_0} \right)^2. \quad (26)$$

Note that the lenslet array typically only covers the inner portion of the overall imaging area, with coverage limited by detector space for recording individual lenslet spectra. Thus, lenslet arrays and, more importantly, their associated detectors can set a tighter constraint on the OWA than the coronagraph.

Read noise is computed using the number of reads per observation,  $N_{\text{read}}$ , the number of contributing pixels, and the read noise counts per pixel,  $R_{\text{e}^-}$ , and is given by

$$c_{\text{R}} = \frac{N_{\text{pix}} N_{\text{read}}}{\Delta t_{\text{exp}}} R_{\text{e}^-}, \quad (27)$$

where dividing by the exposure time,  $\Delta t_{\text{exp}}$ , permits expressing read noise counts as a rate. The number of reads is determined by assuming a maximum exposure time,  $\Delta t_{\text{max}}$  (often limited by cosmic-ray strikes), with

$$N_{\text{read}} = \frac{\Delta t_{\text{exp}}}{\Delta t_{\text{max}}} \quad (28)$$

so that Equation (27) can be written as

$$c_R = \frac{N_{\text{pix}}}{\Delta t_{\text{max}}} R_e^- \quad (29)$$

Note that integer quantities (e.g., numbers of pixels) can be determined by rounding the expressions above, which are, for simplicity, expressed as non-integer quantities.

For completeness, internal thermal noise can be included and has a count rate given by

$$c_{\text{th}} = \pi q \Omega \frac{\lambda}{hc} \epsilon_{\text{sys}} B_{\lambda}(T_{\text{sys}}) \Delta \lambda \left( \frac{D}{2} \right)^2 \\ = \pi q \epsilon_{\text{sys}} B_{\lambda}(T_{\text{sys}}) X^2 \frac{\lambda^4}{4hcR}, \quad (30)$$

where  $\epsilon_{\text{sys}}$  is the effective emissivity for the observing system (of order unity), and  $T_{\text{sys}}$  is the system temperature. As we focus primarily on the visible wavelength range throughout this paper, internal thermal contributions are negligible, so we ignore them throughout.

## References

- Agol, E. 2007, *MNRAS*, **374**, 1271
- Arney, G., Meadows, V., Crisp, D., et al. 2014, *JGRE*, **119**, 1860
- Bean, J. L., Kempton, E. M.-R., & Homeier, D. 2010, *Natur*, **468**, 669
- Beichman, C. A., Woolf, N. J., & Lindensmith, C. A. (ed.) 1999, *The Terrestrial Planet Finder (TPF): A NASA Origins Program to Search for Habitable Planets* (Pasadena, CA: NASA Jet Propulsion Laboratory)
- Boccaletti, A., Schneider, J., Traub, W., et al. 2012, *ExA*, **34**, 355
- Brandt, T. D., & Spiegel, D. S. 2014, *PNAS*, **111**, 13278
- Brown, R. A. 2004, *ApJ*, **607**, 1003
- Brown, R. A. 2005, *ApJ*, **624**, 1010
- Brown, R. A., & Soummer, R. 2010, *ApJ*, **715**, 122
- Burrows, A. 2014, arXiv:1412.6097
- Burrows, A., Sudarsky, D., & Hubeny, I. 2004, *ApJ*, **609**, 407
- Cahoy, K. L., Marley, M. S., & Fortney, J. J. 2010, *ApJ*, **724**, 189
- Charbonneau, D., Brown, T. M., Noyes, R. W., & Gilliland, R. L. 2002, *ApJ*, **568**, 377
- Cockell, C. S., Léger, A., Fridlund, M., et al. 2009, *AsBio*, **9**, 1
- Des Marais, D. J., Harwit, M. O., Jucks, K. W., et al. 2002, *AsBio*, **2**, 153
- Diamond-Lowe, H., Stevenson, K. B., Bean, J. L., Line, M. R., & Fortney, J. J. 2014, *ApJ*, **796**, 66
- Duchêne, G., & Kraus, A. 2013, *ARA&A*, **51**, 269
- Ehrenreich, D., Bonfils, X., Lovis, C., et al. 2014, *A&A*, **570**, A89
- Fraine, J., Deming, D., Benneke, B., et al. 2014, *Natur*, **513**, 526
- Greco, J. P., & Burrows, A. 2015, *ApJ*, **808**, 172
- Grillmair, C. J., Burrows, A., Charbonneau, D., et al. 2008, *Natur*, **456**, 767
- Hansen, C. J., Schwartz, J. C., & Cowan, N. B. 2014, *MNRAS*, **444**, 3632
- Harding, L. K., Demers, R. T., Hoenk, M., et al. 2015, *Proc. SPIE*, **9605**, 14
- Hu, R. 2014, arXiv:1412.7582
- Johnson, J. A., Aller, K. M., Howard, A. W., & Crepp, J. R. 2010, *PASP*, **122**, 905
- Karkoschka, E. 1994, *Icar*, **111**, 174
- Karkoschka, E. 1998, *Icar*, **133**, 134
- Kasting, J. F., Whitmire, D. P., & Reynolds, R. T. 1993, *Icar*, **101**, 108
- Knutson, H. A., Benneke, B., Deming, D., & Homeier, D. 2014a, *Natur*, **505**, 66
- Knutson, H. A., Dragomir, D., Kreidberg, L., et al. 2014b, *ApJ*, **794**, 155
- Kopparapu, R. K., Ramirez, R., Kasting, J. F., et al. 2013, *ApJ*, **765**, 131
- Kouveliotou, C., Agol, E., Batalha, N., et al. 2014, arXiv:1401.3741
- Kreidberg, L., Bean, J. L., Désert, J.-M., et al. 2014, *Natur*, **505**, 69
- Krist, J. E., Shaklan, S. B., & Levine, M. B. 2008, *Proc. SPIE*, **7010**, 44
- Leger, A., Defrere, D., Malbet, F., Labadie, L., & Absil, O. 2015, *ApJ*, **808**, 194
- Leinert, C., Richter, I., Pitz, E., & Planck, B. 1981, *A&A*, **103**, 177
- Levasseur-Regourd, A. C., & Dumont, R. 1980, *A&A*, **84**, 277
- Line, M. R., Knutson, H., Wolf, A. S., & Yung, Y. L. 2014, *ApJ*, **783**, 70
- Lunine, J. I., Fischer, D., Hammel, H., et al. 2008, arXiv:0808.2754
- Madhusudhan, N., & Seager, S. 2009, *ApJ*, **707**, 24
- Maire, A.-L., Galicher, R., Boccaletti, A., et al. 2012, *A&A*, **541**, A83
- Marley, M., Lupu, R., Lewis, N., et al. 2014, arXiv:1412.8440
- Marley, M. S., Gelino, C., Stephens, D., Lunine, J. I., & Freedman, R. 1999, *ApJ*, **513**, 879
- Marois, C., Doyon, R., Racine, R., & Nadeau, D. 2000, *PASP*, **112**, 91
- Mawet, D., Milli, J., Wahhaj, Z., et al. 2014, *ApJ*, **792**, 97
- Meadows, V. S., & Crisp, D. 1996, *JGR*, **101**, 4595
- Misra, A., Meadows, V., Claire, M., & Crisp, D. 2014, *AsBio*, **14**, 67
- Montet, B. T., Crepp, J. R., Johnson, J. A., Howard, A. W., & Marcy, G. W. 2014, *ApJ*, **781**, 28
- Morgan, R., & Siegler, N. 2015, *Proc. SPIE*, **9605**, 21
- Newman, K., Guyon, O., Balasubramanian, K., et al. 2015, *PASP*, **127**, 437
- Papaloizou, J. C. B., Nelson, R. P., Kley, W., Masset, F. S., & Artymowicz, P. 2007, in *Protostars and Planets V, Disk-Planet Interactions during Planet Formation*, ed. B. Reipurth, D. Jewitt, & K. Keil (Tucson, AZ: Arizona Press), 655
- Pont, F., Knutson, H., Gilliland, R., Moutou, C., & Charbonneau, D. 2008, *MNRAS*, **385**, 109
- Roberge, A., Chen, C. H., Millan-Gabet, R., et al. 2012, *PASP*, **124**, 799
- Robinson, T. D., Ennico, K., Meadows, V. S., et al. 2014, *ApJ*, **787**, 171
- Robinson, T. D., Meadows, V. S., & Crisp, D. 2010, *ApJ*, **721**, L67
- Robinson, T. D., Meadows, V. S., Crisp, D., et al. 2011, *AsBio*, **11**, 393
- Savransky, D., Kasdin, N. J., & Cady, E. 2010, *PASP*, **122**, 401
- Schneider, J., Boccaletti, A., Aylward, A., et al. 2008, arXiv:0811.2496
- Sing, D., Désert, J.-M., Lecavelier Des Etangs, A., et al. 2009, *A&A*, **505**, 891
- Sparks, W. B., & Ford, H. C. 2002, *ApJ*, **578**, 543
- Spergel, D., Gehrels, N., Breckinridge, J., et al. 2013, arXiv:1305.5422
- Stark, C. C., Roberge, A., Mandell, A., & Robinson, T. D. 2014, *ApJ*, **795**, 122
- Stark, C. C., Roberge, A., Mandell, A., et al. 2015, *ApJ*, **808**, 149
- Stevenson, K. B., Harrington, J., Nymeyer, S., et al. 2010, *Natur*, **464**, 1161
- Sudarsky, D., Burrows, A., & Hubeny, I. 2003, *ApJ*, **588**, 1121
- Sudarsky, D., Burrows, A., & Pinto, P. 2000, *ApJ*, **538**, 885
- Swain, M. R., Vasisht, G., & Tinetti, G. 2008, *Natur*, **452**, 329
- Swain, M. R., Vasisht, G., Tinetti, G., et al. 2009, *ApJ*, **690**, L114
- Trauger, J., Moody, D., & Gordon, B. 2013, *Proc. SPIE*, **8864**, 12
- Turnbull, M. C., Glassman, T., Roberge, A., et al. 2012, *PASP*, **124**, 418
- Wehrli, C. 1985, *Extraterrestrial Solar Spectrum*, Tech. Rep. No. 615 (Davos-Dorf: World Radiation Center (WRC))